



2000-03

**Applied Computational
Electromagnetics Society Journal /
Volume 15, Number 1**

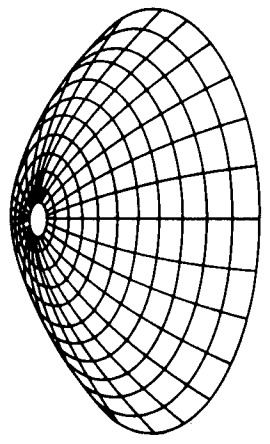
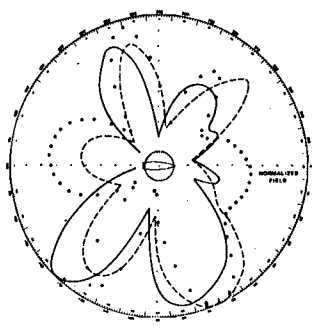
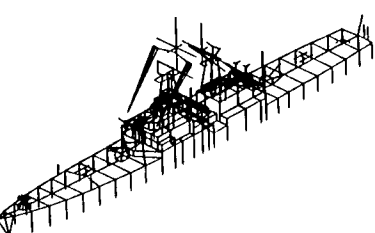
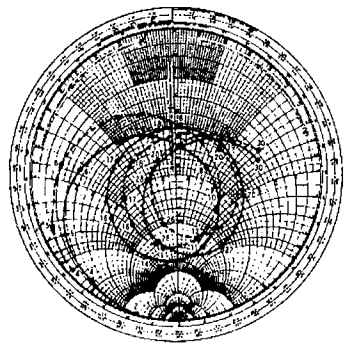
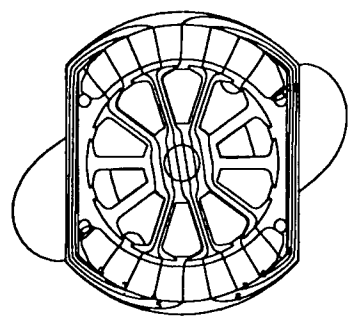
<http://hdl.handle.net/10945/45335>



Calhoun is a project of the Dudley Knox Library at NPS, furthering the precepts and goals of open government and government transparency. All information contained herein has been approved for release by the NPS Public Affairs Officer.

**Dudley Knox Library / Naval Postgraduate School
411 Dyer Road / 1 University Circle
Monterey, California USA 93943**

<http://www.nps.edu/library>



APPLIED
COMPUTATIONAL
ELECTROMAGNETICS
SOCIETY
JOURNAL

March 2000
Vol. 15 No. 1

ISSN 1054-4887

DISTRIBUTION STATEMENT A:
Approved for Public Release -
Distribution Unlimited

20000323 056

GENERAL PURPOSE AND SCOPE. The Applied Computational Electromagnetics Society Journal hereinafter known as the **ACES Journal** is devoted to the exchange of information in computational electromagnetics, to the advancement of the state-of-the-art, and to the promotion of related technical activities. A primary objective of the information exchange is the elimination of the need to "re-invent the wheel" to solve a previously-solved computational problem in electrical engineering, physics, or related fields of study. The technical activities promoted by this publication include code validation, performance analysis, and input/output standardization; code or technique optimization and error minimization; innovations in solution technique or in data input/output; identification of new applications for electromagnetics modeling codes and techniques; integration of computational electromagnetics techniques with new computer architectures; and correlation of computational parameters with physical mechanisms.

SUBMISSIONS. The **ACES Journal** welcomes original, previously unpublished papers, relating to **applied computational electromagnetics**.

Typical papers will represent the computational electromagnetics aspects of research in electrical engineering, physics, or related disciplines. However, papers which represent research in **applied computational electromagnetics** itself are equally acceptable.

Contributions may be sent to the Editors-in-Chief, Dr. Ahmed Kishk or Dr. Allen Glisson

Department of EE

University of Mississippi

University, MS, 38677 USA

Phone: 601-232-5385 (Ahmed)

Phone: 601-232-5353 (Allen)

Fax: 601-232-7231

email:ahmed@olemiss.edu

email:aglisson@mail.olemiss.edu. See "Information for Authors" on inside of back cover.

SUBSCRIPTIONS. All members of the Applied Computational Electromagnetics Society (**ACES**) who have paid their subscription fees are entitled to receive the **ACES Journal** with a minimum of three issues per calendar year.

Visit us on line at: www.emclab.umn.edu/aces, and <http://aces.ee.olemiss.edu>

Back issues, when available, are \$15.00 each. Subscriptions to **ACES**, orders for back issues of the **ACES Journal** and changes of addresses should be sent to:

Dr. Richard W. Adler

ACES Executive Officer

ECE Department, Code ECAB

Naval Postgraduate School

833 Dyer Road, Room 437

Monterey, CA 93943-5121 USA

Allow four week's advance notice for change of address. Claims for missing issues will not be honored because of insufficient notice or address change or loss in mail unless the secretary is notified within 60 days for USA and Canadian subscribers or 90 days for subscribers in other countries, from the last day of the month of publication. For information regarding reprints of individual papers or other materials, see "Information for Authors".

LIABILITY. Neither ACES or the **ACES Journal** editors are responsible for any consequence of misinformation or claims, express or implied, in any published material in an **ACES Journal** issue. This also applies to advertising, for which only camera-ready copies are accepted. Authors are responsible for information contained in their papers. If any material submitted for publication includes material which has already been published elsewhere, it is the author's responsibility to obtain written permission to reproduce such material.

APPLIED
COMPUTATIONAL
ELECTROMAGNETICS
SOCIETY
Journal

March 2000
Vol. 15 No. 1

ISSN 1054-4887

The ACES Journal is abstracted in INSPEC, in Engineering Index, and in DTIC.

The second, third, fourth, and fifth illustrations on the front cover have been obtained from Lawrence Livermore National laboratory.

The first illustration on the front cover has been obtained from FLUX2D software, CEDRAT S.S. France, MAGSOFT Corporation, New York.

THE APPLIED COMPUTATIONAL ELECTROMAGNETICS SOCIETY

JOURNAL EDITORS

EDITOR-IN-CHIEF/ACES

W. Perry Wheless, Jr.
University of Alabama, EE Dept.
PO Box 870286
Tuscaloosa, AL 35487-0286 USA

EDITOR-IN-CHIEF, EMERITUS

Duncan C. Baker
EE Dept. U of Pretoria,
0002 Pretoria, SOUTH AFRICA

MANAGING EDITOR

Richard W. Adler
833 Dyer Rd. Room 437, EC/AB
NPS, Monterey, CA 93943-5121, USA

Ruediger Anders

Applied EM Engineering
Roswell, GA, USA

Brian A. Austin

University of Liverpool
Liverpool, UK

Joao Bastos

University Fed De Santa Catarina
Florianopolis, BRAZIL

John Beggs

Mississippi State University
Mississippi State, MS, USA

Fulvio Bessi

Ingegneria dei Sistemi S.p.A.
Pisa, ITALY

John R. Bowler

University of Surrey
Surrey, UK

John Brauer

Ansoft Corporation
Milwaukee, WI, USA

Tony Fleming

Telecom Australia.
Clayton, Victoria, AUSTRALIA

Pat Foster

Microwave & Antenna Systems
Gt. Malvern, Worc. UK

Gregory R. Haack

DSTO
Salisbury, SA, AUSTRALIA

Christian Hafner

Swiss Federal Inst. of Technology
Zurich, SWITZERLAND

CO-EDITOR-IN-CHIEF/JOURNAL

Ahmed Kishk
University of Mississippi, EE Dept.
University, MS 38677 USA

EDITOR-IN-CHIEF, EMERITUS

Robert M. Bevensee
Box 812
Alamo, CA, 94507-0516 USA

Kueichien C. Hill

Wright Laboratory
Wright-Patterson AFB, OH, USA

Todd H. Hubing

University of Missouri-Rolla
Rolla, MO, USA

Nathan Ida

The University of Akron
Akron, OH, USA

Andrzej Krawczyk

Institute of Electrical Engineering
Warszawa, POLAND

Peter Krylstedt

National Defence Research Est.
Sundbyberg, SWEDEN

Stanley Kubina

Concordia University
Montreal, Quebec, CANADA

Ronald Marhefka

Ohio State University
Columbus, OH, USA

Gerard Meunier

NPG/ENSIEG
St. Martin-d'Heres Cedex, FRANCE

Edmund K. Miller

LASL
Santa Fe, NM, USA

Giorgio Molinari

University of Genova
Genova, ITALY

Frederick A. Molinet

Societe Mothesim
Plessis-Robinson, FRANCE

Gerrit Mur

Technische Universiteit Delft
Delft, NETHERLANDS

CO-EDITOR-IN-CHIEF/JOURNAL

Allen Glisson
University of Mississippi, EE Dept.
University, MS 38677 USA

EDITOR-IN-CHIEF, EMERITUS

David E. Stein
USAF Scientific Advisory Board
Washington, DC 20330 USA

Krishna Naishadham

Wright State University
Dayton, OH, USA

Antonio Orlandi

University of L'Aquila
L'Aquila, ITALY

Giuseppe Pelosi

University of Florence
Florence, ITALY

Andrew F. Peterson

Georgia Institute of Technology
Atlanta, GA, USA

Kurt Richter

Technical University of Graz, IGTE
Graz, AUSTRIA

Harold A. Sabbagh

Sabbagh Associates
Bloomington, IN, USA

Neil R.S. Simons

Communications Research Center
Ottawa, Ontario, CANADA

Norio Takahashi

Okayama University
Tsushima, JAPAN

Yoshiki Uchikawa

Nagoya University
Nagoya, JAPAN

Jean-Claude Verite

Electricite de France
Clamart, Cedex, FRANCE

THE APPLIED COMPUTATIONAL ELECTROMAGNETICS SOCIETY

Vol. 15 No. 1

March 2000

TABLE OF CONTENTS

"EMAPS: A 3D Hybrid Fem/Mom Code" Y. Ji and T. Hubing.....	1
"A Hybrid MoM/FEM Technique for Scattering from a Complex BOR with Appendages" AndrewD. Greenwood and Jianming Jin	13
"Impedance of a Half-Wave Dipole Over a Finite Ground Plane" P.R. Foster and R.A. Burberry	21
"The Design of Planar Slot Arrays Revisited" J.C. Coetzee and J. Joubert	27

© 2000, The Applied Computational Electromagnetics Society

EMAP5: A 3D HYBRID FEM/MOM CODE

Y. Ji and T. Hubing
Department of Electrical and Computer Engineering
University of Missouri-Rolla
Rolla, MO 65401

Abstract--EMAP5 is a numerical software package designed to model electromagnetic problems. It employs the finite element method (FEM) to analyze a volume, and employs the method of moments (MoM) to analyze the region exterior to the FEM volume. The two methods are coupled by enforcing the continuity of the tangential fields on the interface. Dielectrics, lossy dielectrics and metal objects can be modeled within the FEM volume. Metal objects can also be located exterior to, or on the surface of the FEM volume. A simple input file translator (SIFT) is provided with EMAP5 that allows users to define basic input configurations on a rectangular grid without a graphical interface. It is also possible to use commercial mesh generators to analyze more complex geometries of arbitrary shape. EMAP5 can model three types of sources: incident plane waves, voltage sources on metal patches and impressed current sources in the finite element region. This paper describes the implementation of EMAP5 and provides four examples to demonstrate the range of configurations that EMAP5 is capable of modeling using the SIFT translator.

I. INTRODUCTION

Methods used to solve Maxwell's equations can often be classified into one of two categories. One category is integral equation-based methods. Integral equation-based methods generally solve for unknown fields or currents on the surface of homogeneous volumes. Only the surfaces are meshed; therefore the number of unknowns is relatively small. Integral equation-based methods are well suited for modeling homogeneous structures in unbounded geometries.

The other category is partial differential equation (PDE)-based methods. PDE-based methods require a volume mesh. The resulting number of unknowns is usually much higher than that obtained from integral equation-based methods, but the reduced complexity of the solution method can more than compensate for this. PDE-based methods are well suited for modeling complex inhomogeneous structures, particularly those in bounded geometries (e.g. a waveguide or a metallic enclosure).

The finite element method (FEM) is a powerful PDE-based method. It requires the entire region of interest to be meshed. However, each mesh element can have its own electromagnetic properties (ϵ , μ , σ).

Thus, FEM has an inherent capacity to analyze inhomogeneous structures. In addition, FEM does not require a uniform mesh. Various types of elements, for example, bricks, tetrahedra and prisms, can be used to discretize arbitrary geometric configurations. Therefore, FEM is well suited for modeling complex, inhomogeneous structures. A significant disadvantage of the FEM method is the inability to model unbounded geometries without using absorbing boundary elements. Absorbing boundary elements are not effective when they closely conform to the shape of long thin objects (e.g. cables). When modeling objects with one dimension significantly longer than the others using FEM, it is generally necessary to fill the empty space around these objects with many elements that transition from the object of interest to the absorbing boundary. This can significantly inflate the overall size of the problem.

The method of moments is not actually an electromagnetic modeling technique, but rather it is a technique for solving complex linear equations [1, 2]. However, electromagnetic modeling techniques that apply the method of moments to the solution of electric or magnetic field integral equations are generally referred to as method-of-moment (MoM) techniques. MoM techniques can be used to model metallic (particularly wire) structures in unbounded geometries very effectively.

In order to take advantage of the strengths of both the FEM and MoM methods, several researchers have developed hybrid FEM/MoM approaches [3-6]. Hybrid FEM/MoM methods generally take advantage of the FEM's ability to model complex inhomogeneous structures and the MoM's ability to model unbounded geometries. The specific strengths of a particular code depend on the details of the implementation, particularly the form of the integral equation and the basis and weighting functions employed.

EMAP5 (ElectroMagnetic Analysis Program version 5) is a hybrid FEM/MoM modeling code developed at the University of Missouri-Rolla (UMR). EMAP5 was developed in order to demonstrate and validate the hybrid technique described in [6,7]. This technique, used in conjunction with a mesh generator, is particularly useful for analyzing EMI from printed circuit board geometries with enclosures or attached cables. A rudimentary mesh generator (SIFT5) is distributed with the EMAP5 code. This non-graphical

user interface is simple and portable, making it a good tool for educators and people who want to learn to use the EMAP5 code. However, the meshes generated by the SIFT5 code do not exploit the primary advantage of FEM modeling codes (i.e. the ability to adapt the size and shape of the mesh to fit the geometry). The EMAP5 and SIFT5 source codes can be obtained via the web at <<http://www.emclab.umr.edu/emap5>>.

II. FORMULATION

Although details of the EMAP5 formulation are described in [6,7], a brief summary is provided below. The general structure of interest is shown in Figure 1. A dielectric volume V_2 has electrical properties (ϵ_2, μ_2) and is enclosed by a surface S_2 . A conductive volume V_3 is enclosed by a conductive surface S_c . The fields within V_3 vanish. V_1 denotes the volume outside of V_2 and V_3 , which is assumed to be free space. ($\mathbf{E}_1, \mathbf{H}_1$) and ($\mathbf{E}_2, \mathbf{H}_2$) denote the electric and magnetic fields in V_1 and V_2 , respectively. The unit normal vectors for S_2 and S_c are defined pointing outward toward V_1 . The structure is excited by an incident wave ($\mathbf{E}^{inc}, \mathbf{H}^{inc}$) or impressed sources ($\mathbf{J}^{int}, \mathbf{M}^{int}$). The scattered electric and magnetic fields are ($\mathbf{E}^s, \mathbf{H}^s$). The objective is to solve for the scattered fields ($\mathbf{E}^s, \mathbf{H}^s$) or the surface electric current density on S_c .

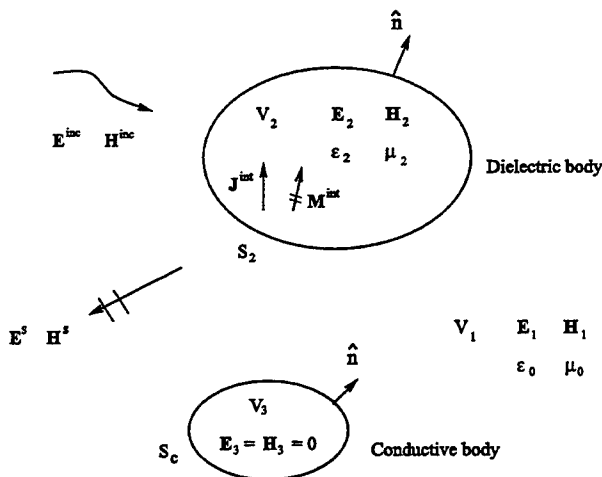


Figure 1. A dielectric object and a conductive object illuminated by ($\mathbf{E}^{inc}, \mathbf{H}^{inc}$) or ($\mathbf{J}^{int}, \mathbf{M}^{int}$).

From Maxwell equations, the vector Helmholtz equation in terms of \mathbf{E} can be written as,

$$\begin{aligned} \nabla \times \left(\frac{\nabla \times \mathbf{E}(\mathbf{r})}{j\omega \mu_0 \mu_r} \right) + j\omega \epsilon_0 \epsilon_r \mathbf{E}(\mathbf{r}) \\ = -\mathbf{J}^{int}(\mathbf{r}) - \frac{1}{j\omega \mu_0 \mu_r} \nabla \times \mathbf{M}^{int}(\mathbf{r}). \end{aligned} \quad (1)$$

After multiplying Equation (1) by a weighting function $\mathbf{w}(\mathbf{r})$ and integrating over the finite element domain V_2 , one obtains the FEM weak form as follows [8, 9],

$$\begin{aligned} \int_{V_2} \left[\frac{(\nabla \times \mathbf{E}(\mathbf{r})) \cdot (\nabla \times \mathbf{w}(\mathbf{r}))}{j\omega \mu_0 \mu_r} + j\omega \epsilon_0 \epsilon_r \mathbf{E}(\mathbf{r}) \cdot \mathbf{w}(\mathbf{r}) \right] dV \\ = \int_{S_2} (\hat{\mathbf{n}} \times \mathbf{H}(\mathbf{r})) \cdot \mathbf{w}(\mathbf{r}) dS \\ - \int_{V_2} \left[\mathbf{J}^{int}(\mathbf{r}) + \frac{1}{j\omega \mu_0 \mu_r} \nabla \times \mathbf{M}^{int}(\mathbf{r}) \right] \cdot \mathbf{w}(\mathbf{r}) dV \end{aligned} \quad (2)$$

Equation (2) can also be derived using the variational method [10] (pp. 158-161), [11] (pp. 158-160).

Within volume V_2 , EMAP5 uses the vector tetrahedral elements proposed by Barton and Cendes [10] (pp. 56-59), [12]. Each basis function is defined within a tetrahedron, and is associated with one of the six edges. The electric field \mathbf{E} within volume V_2 can be expanded as,

$$\mathbf{E}(\mathbf{r}) = \sum_{n=1}^{N_v} E_n \mathbf{w}_n(\mathbf{r}) \quad (3)$$

where N_v is the total number of interior edges and boundary edges on the dielectric surface, and $\{E_n\}$ is a set of unknown complex scalar coefficients.

The surface integral term in Equation (2) can be evaluated by using a surface basis function $\mathbf{f}(\mathbf{r})$, which is discussed later. The weighting functions chosen are $\mathbf{w}_n(\mathbf{r})$, $n=1 \dots N_v$. After multiplying by the weighting functions, Equation (2) can be discretized as,

$$\begin{bmatrix} A_{ii} & A_{id} \\ A_{di} & A_{dd} \end{bmatrix} \begin{bmatrix} E_i \\ E_d \end{bmatrix} = \begin{bmatrix} 0 & 0 \\ 0 & B_{dh} \end{bmatrix} \begin{bmatrix} 0 \\ J_h \end{bmatrix} + [g^{int}] \quad (4)$$

The unknown coefficients $[E_n]$ are partitioned according to edge type. The two categories are interior edges, which are denoted by the subscript i in Equation (4), and dielectric boundary edges, which are denoted by the subscript d in Equation (4). $[J_h]$ is a set of unknown complex scalar coefficients for the surface electric current densities on S_d . S_d is defined as S_2 if the conductive body is not adjacent to the dielectric body; otherwise, $S_d = S_2 - (S_2 \cap S_c)$. Edges in $[J_h]$ include dielectric boundary edges and junction edges (i.e. edges that are on both the conductor and dielectric boundary). $[B_{dh}]$ is a square matrix if there are no junction edges in the problem. $[g^{int}]$ is the source term, representing sources located within the FEM region. The elements of $[A]$, $[B_{dh}]$, and $[g^{int}]$ are given by,

$$A_{mn} = \int_{V_2} \left[\frac{(\nabla \times \mathbf{w}_n(\mathbf{r})) \cdot (\nabla \times \mathbf{w}_m(\mathbf{r}))}{j\omega\mu_0\mu_r + j\omega\varepsilon_0\varepsilon_r \mathbf{w}_n(\mathbf{r}) \cdot \mathbf{w}_m(\mathbf{r})} \right] dV \quad (5)$$

$$B_{mn} = \int_{S_d} \mathbf{f}_n(\mathbf{r}) \cdot \mathbf{w}_m(\mathbf{r}) dS \quad (6)$$

$$g_m^{\text{int}} = - \int_{V_2} \left[\mathbf{J}^{\text{int}} + \frac{1}{j\omega\mu_0\mu_r} (\nabla \times \mathbf{M}^{\text{int}}) \right] \cdot \mathbf{w}_m(\mathbf{r}) dV \quad (7)$$

where $\mathbf{f}_n(\mathbf{r})$ is the surface basis function. Since the tangential \mathbf{E} field vanishes on S_c , B_{mn} is evaluated over S_d rather than all of S_2 . A detailed description of how to evaluate the terms in Equation (5) is provided in [11] (pp. 254-257). Appendix A describes how to evaluate Equation (6). $[g_m^{\text{int}}]$ is the source term and is discussed in a later section.

The MoM surface integral equation evaluated by the MoM part of EMAP5 is a form of the electric field integral equation (EFIE) [13],

$$\begin{aligned} \mathbf{E}^{\text{inc}}(\mathbf{r}) = & \frac{1}{2} \mathbf{E}(\mathbf{r}) + \int_S \{ \mathbf{M}(\mathbf{r}') \times \nabla' G_0(\mathbf{r}, \mathbf{r}') \\ & + j k_0 \eta_0 \mathbf{J}(\mathbf{r}') G_0(\mathbf{r}, \mathbf{r}') \\ & - j \frac{\eta_0}{k_0} \nabla' \cdot \mathbf{J}(\mathbf{r}') \nabla' G_0(\mathbf{r}, \mathbf{r}') \} dS' \end{aligned} \quad (8)$$

where $\mathbf{r} \in S$, $S \equiv S_c \cup S_2$, η_0 and k_0 are the intrinsic impedance and wavenumber in free space, respectively, and

$$G_0(\mathbf{r}, \mathbf{r}') = \frac{e^{-jk_0|\mathbf{r}-\mathbf{r}'|}}{4\pi|\mathbf{r}-\mathbf{r}'|} \quad (9)$$

is the Green's function in free space. The integral term with a bar in Equation (8) denotes a principal-value integral. The singularity at $\mathbf{r}=\mathbf{r}'$ is excluded. The equivalent surface electric and magnetic currents are defined as,

$$\mathbf{J}(\mathbf{r}) = \hat{\mathbf{n}} \times \mathbf{H}(\mathbf{r}), \quad \mathbf{r} \in S \quad (10)$$

$$\mathbf{M}(\mathbf{r}) = \mathbf{E}(\mathbf{r}) \times \hat{\mathbf{n}}, \quad \mathbf{r} \in S_d. \quad (11)$$

$\mathbf{M}(\mathbf{r})$ vanishes on S_c . $\mathbf{J}(\mathbf{r})$ and $\mathbf{M}(\mathbf{r})$ can be approximated by using the triangular basis function $\mathbf{f}_n(\mathbf{r})$ proposed by Glisson [14]. On the surface S_d , the MoM basis function $\mathbf{f}_n(\mathbf{r})$ and the FEM basis function $\mathbf{w}_n(\mathbf{r})$ are related by,

$$\mathbf{w}_n(\mathbf{r}) = \hat{\mathbf{n}} \times \mathbf{f}_n(\mathbf{r}), \quad \mathbf{r} \in S_d \quad (12)$$

$\mathbf{J}(\mathbf{r})$, $\mathbf{M}(\mathbf{r})$ can be expanded as,

$$\mathbf{J}(\mathbf{r}) = \sum_{n=1}^{N_s} J_n \mathbf{f}_n(\mathbf{r}) \quad (13)$$

$$\mathbf{M}(\mathbf{r}) = \sum_{n=1}^{N_d} E_n \mathbf{f}_n(\mathbf{r}) \quad (14)$$

where N_s is the total number of edges on the surface S , and N_d is the total number of edges on the surface S_d . $\{J_n\}$ and $\{E_n\}$ are unknown complex scalar coefficients.

The weighting functions chosen are $\mathbf{f}_n(\mathbf{r})$, $n=1, \dots, N_s$. After multiplying by the weighting functions, Equation (8) can be discretized into Equation (15), which is a matrix equation. Edges on S_d and S_c are grouped together respectively.

$$\begin{bmatrix} C_{hh} & C_{hc} \\ C_{ch} & C_{cc} \end{bmatrix} \begin{bmatrix} J_h \\ J_c \end{bmatrix} = \begin{bmatrix} D_{hd} & 0 \\ D_{cd} & 0 \end{bmatrix} \begin{bmatrix} E_d \\ 0 \end{bmatrix} - \begin{bmatrix} F_h^i \\ F_c^i \end{bmatrix}. \quad (15)$$

The elements in matrices $[C]$, $[D]$ and $[F^i]$ are given by,

$$\begin{aligned} C_{mn} = & -jk_0\eta_0 \int_{S_m} \mathbf{f}_m(\mathbf{r}) \cdot \left[\int_{S_n} \mathbf{f}_n(\mathbf{r}') G_0(\mathbf{r}, \mathbf{r}') dS' \right] dS \\ & + j \frac{\eta_0}{k_0} \int_{S_m} \mathbf{f}_m(\mathbf{r}) \cdot \left[\int_{S_n} (\nabla' \cdot \mathbf{f}_n(\mathbf{r}')) \nabla' G_0(\mathbf{r}, \mathbf{r}') dS' \right] dS \end{aligned} \quad (16)$$

$$\begin{aligned} D_{mn} = & \int_{S_m} \mathbf{f}_m(\mathbf{r}) \cdot \\ & \left[\int_{S_n} \mathbf{f}_n(\mathbf{r}') \times \nabla' G_0(\mathbf{r}, \mathbf{r}') dS' + \frac{1}{2} \mathbf{w}_n(\mathbf{r}) \right] dS \end{aligned} \quad (17)$$

$$F_m^i = \int_{S_m} \mathbf{f}_m(\mathbf{r}) \cdot \mathbf{E}^{\text{inc}}(\mathbf{r}) dS. \quad (18)$$

Details of how to evaluate Equation (16) are provided in [14]. Appendix B describes how to evaluate Equation (17). Equation (18) can be evaluated by using the Gaussian Quadrature technique.

From Equation (15), $[J_h]$ can be expressed as,

$$\begin{bmatrix} 0 \\ J_h \end{bmatrix} = \begin{bmatrix} 0 & 0 \\ 0 & C_{hh}^{-1} D'_{hd} \end{bmatrix} \begin{bmatrix} 0 \\ E_d \end{bmatrix} + \begin{bmatrix} 0 \\ C_{hh}^{-1} K \end{bmatrix} \quad (19)$$

where

$$C'_{hh} \equiv C_{hh} - C_{hc} C_{cc}^{-1} C_{ch} \quad (20)$$

$$D'_{hd} \equiv D_{hd} - C_{hc} C_{cc}^{-1} D_{cd} \quad (21)$$

$$K \equiv C_{hc} C_{cc}^{-1} F_c^i - F_h^i. \quad (22)$$

After combining Equations (4) and (19), the final matrix equation that must be solved is given by,

$$\left([A] + \begin{bmatrix} 0 & 0 \\ 0 & -B_{dh} C_{hh}^{-1} D'_{hd} \end{bmatrix} \right) \begin{bmatrix} E_i \\ E_d \end{bmatrix} = [g^{int}] + \begin{bmatrix} 0 \\ B_{dh} C_{hh}^{-1} K \end{bmatrix} \quad (23)$$

where $[A]$ is the FEM matrix in Equation (4), and $B_{dh} C_{hh}^{-1} D'_{hd}$ is the coupled matrix from the MoM equation. The right-hand side in Equation (23) is the source term.

The far fields can be calculated using the equivalent surface currents \mathbf{J} and \mathbf{M} defined in Equations (10) and (11). The point of observation is denoted by (r, θ, φ) in spherical coordinates. Potential functions \mathbf{A} and \mathbf{F} can be approximated by [15],

$$\begin{aligned} \mathbf{A}(\mathbf{r}) &\equiv \frac{e^{-jk_0 r}}{4\pi r} \int_S \mathbf{J}(\mathbf{r}') e^{jk_0 r' \cos\psi} dS' \\ &= \frac{e^{-jk_0 r}}{4\pi r} \sum_n J_n \int_{S_n} \mathbf{f}_n(\mathbf{r}') e^{jk_0 r' \cos\psi} dS' \end{aligned} \quad (24)$$

$$\begin{aligned} \mathbf{F}(\mathbf{r}) &\equiv \frac{e^{-jk_0 r}}{4\pi r} \int_S \mathbf{M}(\mathbf{r}') e^{jk_0 r' \cos\psi} dS' \\ &= \frac{e^{-jk_0 r}}{4\pi r} \sum_n E_n \int_{S_n} \mathbf{f}_n(\mathbf{r}') e^{jk_0 r' \cos\psi} dS' \end{aligned} \quad (25)$$

where $r' \cos\psi = x' \cos\varphi \sin\theta + y' \sin\varphi \sin\theta + z' \cos\theta$. EMAP5 evaluates the integral terms in Equations (24) and (25) using the Gaussian Quadrature technique. The far fields are given by [15],

$$E_\theta = (-j k_0 \eta_0) (A_\theta + \frac{F_\theta}{\eta_0}) \quad (26)$$

$$E_\varphi = (-j k_0 \eta_0) (A_\varphi - \frac{F_\varphi}{\eta_0}). \quad (27)$$

III. SOURCE AND LOAD MODELING

EMAP5 can model voltage sources on metal patches, incident plane waves, and impressed current sources within the FEM region. A delta-gap voltage source can be defined anywhere on the MoM surface. It can be modeled as an incident E-field normal to edges coinciding with the source [9] (pp. 260-261). A delta-gap voltage source parallel to the x-axis can be expressed as,

$$\mathbf{E}^{inc} = V \delta(x - x_f) \hat{x} \quad (28)$$

where x_f is the location of the source and V is the voltage magnitude, and $\delta(x)$ is the Dirac delta function. Suppose that edge m coincides with the source. The normal component of $\mathbf{f}_m(\mathbf{r})$ across edge m is unity. Thus, the source term given by Equation (18) is,

$$F_m^i = V l_m \quad (29)$$

where l_m is the length of edge m .

Plane wave sources are also described using the forcing term given by Equation (18). Assume the incident wave can be expressed in a spherical coordinate system as,

$$\mathbf{E}^{inc} = (E_\theta \hat{\theta} + E_\varphi \hat{\varphi}) e^{-j\mathbf{k}\cdot\mathbf{r}} \quad (30)$$

where the propagation vector \mathbf{k} is,

$$\mathbf{k} = k(\sin\theta \cos\varphi \hat{x} + \sin\theta \sin\varphi \hat{y} + \cos\theta \hat{z}) \quad (31)$$

and (θ, φ) defines the angle of the propagation direction of the plane wave. EMAP5 calculates the E field of the plane wave on the surface of the structure, then evaluates the right-hand side of Equation (18) numerically.

EMAP5 uses current filaments on tetrahedron edges to model sources located within the FEM region [11] (pp. 324-325). A current source along the z-axis can be expressed as,

$$\mathbf{J}^{int} = I \delta(x - x_f) \delta(y - y_f) \hat{z} \quad (32)$$

where (x_f, y_f) specifies its position, I denotes the electric current magnitude, and $\delta(x)$ is the Dirac delta function. The contribution to vector $[g^{int}]$ in Equation (7) is simply,

$$g^{int} = I l \iint \hat{z} \cdot \{W\} \delta(x - x_f) \delta(y - y_f) dx dy \quad (33)$$

where l is the edge length and $\{W\}$ is the weighting function. According to the expression in Equation (33), only edges coinciding with a current source have non-zero components in the $[g^{int}]$ vector. After the E-fields along the current source edges are obtained, the voltage drop across the source can be calculated. Thus, the input impedance Z_{in} can be obtained. The desired fields under an excitation of any magnitude voltage V_{in} can be obtained by multiplying the factor V_{in}/Z_{in} to the results obtained when I is set to one Ampere.

EMAP5 models load impedances Z_L as dielectric posts on tetrahedron edges. These posts have a finite conductivity given by,

$$\sigma = \frac{l}{Z_L S} \quad (34)$$

where l is its length, and S is the cross sectional area. If the load is treated as a lumped element, its contribution to the finite element matrix is as follows [11] (pp. 324-325),

$$[A^e] = \frac{l^2}{Z_L} \iint \{W\} \{W\}^T \delta(x - x_L)(y - y_L) dx dy \quad (35)$$

where (x_L, y_L) is the position of the impedance load.

IV. MATRIX EQUATION SOLVER

EMAP5 uses the complex bi-conjugate gradient method (CBCG) to solve the final complex matrix equation, Equation (23). The major advantage of CBCG lies in its iterative nature and its ability to use the row-indexed method to store sparse matrices efficiently. The CBCG method was first introduced by Jacobs [16]. A brief outline of the algorithm is provided in the following section.

A. Complex Bi-Conjugate Gradient Method

Consider a complex matrix equation,

$$[M][x]=[b] \quad (36)$$

where $[M]$ is an $N \times N$ complex matrix, and $[b]$ and $[x]$ are order- N complex column vectors. Both $[M]$ and $[b]$ are known while $[x]$ is unknown. Four column vectors are defined as,

1. the residue, r ,
2. the bi-residue, \bar{r} ,
3. the direction vector, p ,
4. the bi-direction vector, \bar{p} .

These vectors are initialized as,

$$r_0 = p_0 = b \quad (37)$$

$$\bar{r}_0 = \bar{p}_0 = b^* \quad (38)$$

where $*$ denotes the complex conjugate. The Hermitian conjugate of M is,

$$M^H \equiv (M^*)^T \quad (39)$$

where T denotes transpose. The inner product of two complex column vectors is defined as,

$$\langle p_1, p_2 \rangle \equiv (p_1^*)^T p_2 \quad (40)$$

The following steps are repeated N times at most. For $k=0, \dots, N-1$, calculate the step-length parameter,

$$\alpha_k = \frac{\langle \bar{r}_k, r_k \rangle}{\langle p_k, M p_k \rangle} \quad (41)$$

The new solution estimate then becomes,

$$x_{k+1} = x_k + \alpha_k p_k \quad (42)$$

The new residue and bi-residue are calculated as,

$$r_{k+1} = r_k - \alpha_k M p_k \quad (43)$$

$$\bar{r}_{k+1} = \bar{r}_k - \alpha_k^* M^H \bar{p}_k \quad (44)$$

The bi-conjugate coefficient is calculated using the following formula,

$$\beta_k = - \frac{\langle M^H \bar{p}_k, r_{k+1} \rangle}{\langle p_k, M p_k \rangle} \quad (45)$$

The new direction and bi-direction vectors are given by,

$$p_{k+1} = r_{k+1} + \beta_k p_k \quad (46)$$

$$\bar{p}_{k+1} = \bar{r}_{k+1} + \beta_k^* \bar{p}_k \quad (47)$$

This iteration is continued until a termination condition is satisfied,

$$\frac{\|r_k\|_2}{\|b\|_2} \leq \text{TOL} \quad (48)$$

where TOL is a number defining the tolerance. The best value of TOL depends on the problem for EMAP5. Typically, 1×10^{-3} is sufficient. The value of TOL is defined as a macro in the EMAP5 source code so it can be easily adjusted by the user.

B. Implementation

It is not necessary to explicitly add the two matrices on the left-hand side of Equation (23) in CBCG. The FEM matrix $[A]$ is a sparse and symmetric matrix. The row-indexed scheme [17] is used to store it. The MoM coupled matrix is an asymmetric compact matrix. A full 2D array is used to store it. These two matrices are stored separately in order to make it is easier to obtain the Hermitian of the left-hand matrix. Since $[A]$ is symmetric,

$$A^H = (A^T)^* = A^* \quad (49)$$

Thus, it is not necessary to search the non-zero elements column by column in $[A]$ when Hermitian operations are present. Instead, the search is done row by row. The row-indexed scheme is very efficient in this case. While the coupled MoM matrix is not symmetric, exchanging its row index and column index will result in its transpose.

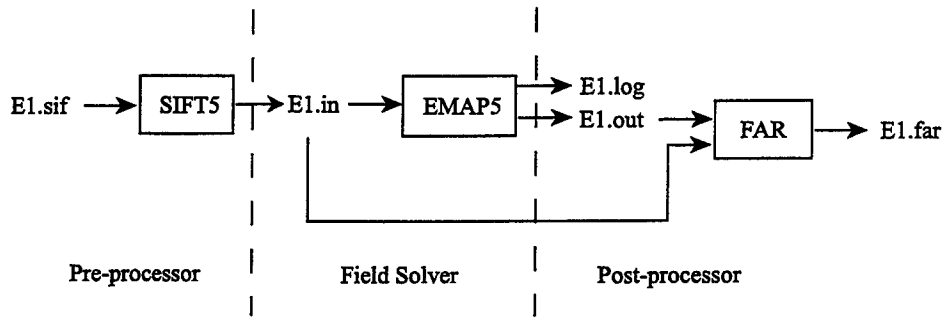


Figure 2. Components of the EMAP5 package.

C. Accuracy and Convergence Problem

Although the CBCG solver conserves memory, it is an iterative method and it may have difficulty converging in some situations. Convergence problems may result from round-off errors. Usually the round-off error for single-precision data is 1.19×10^{-7} [17]. If the total number of unknown edges is 1,000, the average error due to round-off errors is

$$\sqrt{1,000} \times 1.19 \times 10^{-7} \approx 3.8 \times 10^{-6}.$$

In the worst case, the error is $1,000 \times 1.19 \times 10^{-7} = 1.19 \times 10^{-4}$. Because the total round-off error could be very large, it is impractical to set the TOL in Equation (48) to be on the order of 10^{-4} if no special technique, such as pre-conditioning, is used to reduce the total round-off error. The round-off error of double-precision data is 2.22×10^{-16} [17]. If double precision is used for the matrix calculations, round-off errors will not reduce the effectiveness of CBCG considerably. In EMAP5, all data are stored in double precision; however, double precision numbers require twice as much as memory to store as single precision.

Another potential difficulty with the CBCG solver arises when the algorithm becomes unstable. This can happen when the denominator of the expressions for α_k and β_k is close to zero. EMAP5 monitors the value of the denominator. If it becomes too small, EMAP5 will restart the algorithm using the current solution as the initial estimate as suggested by Jacobs [16].

V. COMPONENTS OF EMAP5

EMAP5 is written in ANSI C. Thus, it can be compiled without modification on many computer platforms. As shown in Figure 2, the EMAP5 software package includes three major components: SIFT5, EMAP5 and FAR. EMAP5 was developed for research and educational use. It does not have a sophisticated mesh generator or graphical visualization tools. SIFT5 can be used to describe simple input geometries with a rectangular grid. It is also possible to use commercial

mesh generators to analyze more complex geometries of arbitrary shape. EMAP5 is the FEM/MoM field solver. FAR calculates far-field electric fields from the equivalent surface currents calculated by EMAP5.

Standard Input File Translator version 5 (SIFT5) is designed to generate input files for the field solver EMAP5. SIFT5 reads a text file in the SIFT format [18-20] and generates an input file for EMAP5. Users can describe the structure of interest by using eleven keywords. The physical geometry of the structure, source type and location, and the geometry of areas in which fields are to be printed by the solver, must be specified.

EMAP5 is the hybrid FEM/MoM field solver. It reads an input file generated by SIFT5. A .log file is generated to log running status and error messages. The log file was initially designed to debug the code, but users can also benefit from log messages. EMAP5 will print out fields within areas specified by the .sif file, to one or more output files. All equivalent surface currents \mathbf{J} and \mathbf{M} must be printed to a file if the user needs to calculate far fields.

FAR is a program used to calculate the far field radiation pattern. FAR needs two input files. One is the file generated by SIFT5 and the other contains the equivalent surface currents \mathbf{J} and \mathbf{M} . The FAR program will prompt users to input the observing distance R in wavelengths, the observing θ interval in degrees, and the observing ϕ interval in degrees.

VI. STRUCTURE OF EMAP5

Figure 3 shows a flowchart for the field solver EMAP5. Descriptions of the functions used by EMAP5 are provided below,

- ReadInputFile()

reads an input file generated by SIFT5, and checks whether the input file is consistent (i.e. the input makes sense). If not, it aborts the program and reports problems with the input to the user.

- **ComputeBMatrix()**
places a 3×3 sub-matrix (corresponding to one observing triangular patch and one source triangular patch) into the global B matrix based on the local-to-global mapping.
- **ComputeCMatrix()**
places a 3×3 sub-matrix into the global C matrix based on the local-to-global mapping.
- **ComputeDMatrix()**
places a 3×3 sub-matrix into the global D matrix based on the local-to-global mapping.
- **ComputeCorrectionTerm()**
uses B, C, and D matrices to compute the MoM coupling matrix. It also creates the necessary matrices required to compute the equivalent surface currents.
- **FEMMatrixCompute()**
computes a 6×6 matrix for each tetrahedron first, then assembles the global matrix based on the local-to-global mapping. The matrix is stored using the row-indexed method.
- **CreateRHSVector()**
creates the RHS (right-hand side) vector of the final matrix equation.
- **ConjugateSolver()**
uses the Complex Bi-Conjugate Gradient Method to solve the final matrix equation. For MoM-only analyses, this function can be replaced with an LU decomposition solver.
- **SurfaceFieldCompute()**
computes the equivalent surface currents on the boundary.
- **PrintOutput()**
outputs the values of fields in regions specified by the input file to a file specified by the input file. All equivalent surface electric and magnetic currents must be written to a file if users are interested in the far field pattern.

VII. NUMERICAL RESULTS

This section describes four example geometries that can be solved using the EMAP5 software package. Each geometry is described in sufficient detail to allow others to duplicate the analysis. Results obtained from EMAP5 are compared to results obtained using other well-established codes, measurements, or analytical results.

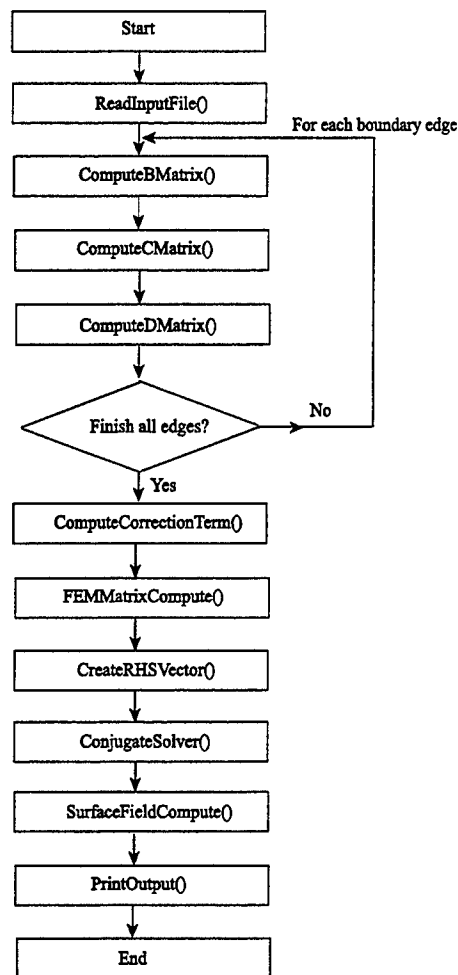


Figure 3. EMAP5 flowchart.

The first example analyzes the electromagnetic scattering from a square plate over a dielectric slab. As shown in Figure 4, the configuration consists of a square plate of dimension $0.75\lambda \times 0.75\lambda$, and a dielectric slab of $\epsilon_r = 2.0$, and dimensions of $0.4\lambda \times 0.4\lambda \times 0.2\lambda$. The plate is symmetrically placed above the slab. The distance between the plate and the dielectric slab is 0.15λ . The system is illuminated by an x-polarized, +z traveling plane wave. In EMAP5's hybrid solution, the dielectric is divided into 320 tetrahedra. The surface of the dielectric and the metal plate are divided into 392 triangle patches. Figure 5 shows the normalized far field pattern calculated by EMAP5. For comparison, the results obtained by Arvas *et al.* [21] have been plotted on the same scale. The authors in [21] used a method of moments technique, which is based on a combined field integral equation formulation. As is evident from the figure, the two solutions compare very well.

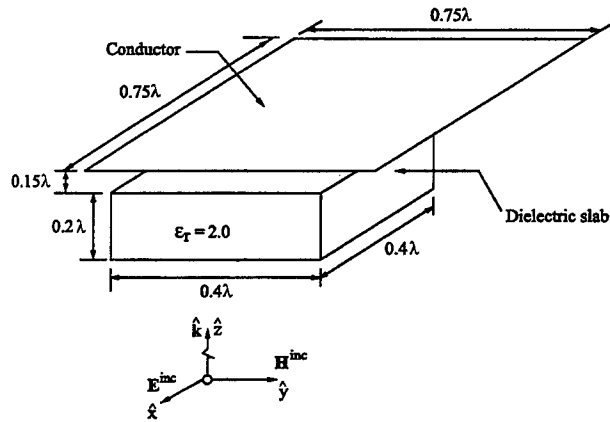


Figure 4. A conducting plate over a dielectric slab.

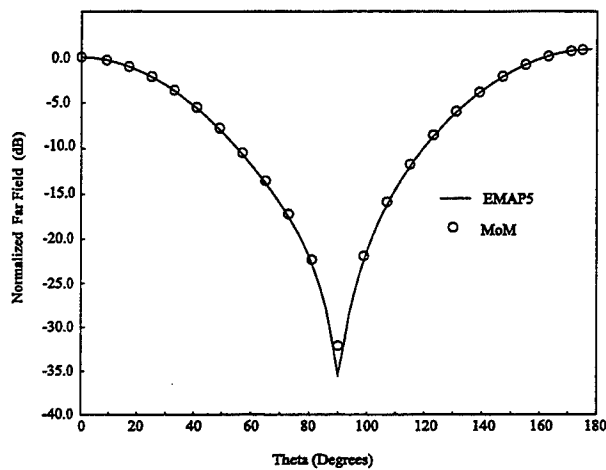


Figure 5. The normalized far field pattern for the configuration in Figure 4.

The second example demonstrates the application of the EMAP5 code in modeling microstrip geometries. The geometry of the structure is shown in Figure 6. The board is made of a dielectric with $\epsilon_r=4.0$. The trace is excited by a source at one end, and is terminated by a resistor at the other end. Microstrip lines support quasi-TEM fields [22] (pp. 160-161) and can therefore be viewed as transmission lines. The input impedance Z_{in} of a transmission line is given by,

$$Z_{in} = Z_0 \frac{Z_L + j Z_0 \tan(\beta l)}{Z_0 + j Z_L \tan(\beta l)} \quad (50)$$

where Z_L is the load impedance, β is the propagation constant; l is the length of the transmission line. To determine the characteristic impedance Z_0 of the transmission line, one can find the input impedance when the load side is shorted or open, respectively. When the load side is shorted, the input impedance is given by,

$$(Z_{in})_{short} = j Z_0 \tan(\beta l). \quad (51)$$

When the load side is open, the input impedance is given by,

$$(Z_{in})_{open} = -j \frac{Z_0}{\tan(\beta l)}. \quad (52)$$

Thus, the characteristic impedance is given by,

$$Z_0 = \sqrt{(Z_{in})_{short} (Z_{in})_{open}}. \quad (53)$$

In EMAP5's hybrid solution, the dielectric volume is divided into 900 tetrahedra. The surface is divided into 828 triangles. Table 1 lists $(Z_{in})_{open}$, $(Z_{in})_{short}$ and Z_0 obtained using EMAP5 at three different frequencies. The results in Table 1 are consistent and $Z_0 = 56.4$ Ohms at each frequency. Figure 7 shows the input impedance at the source end obtained by EMSIM [23] when the trace is terminated with a 56.4Ω resistor. It is evident that the microstrip line is almost perfectly matched confirming EMAP5's calculation of the characteristic impedance.

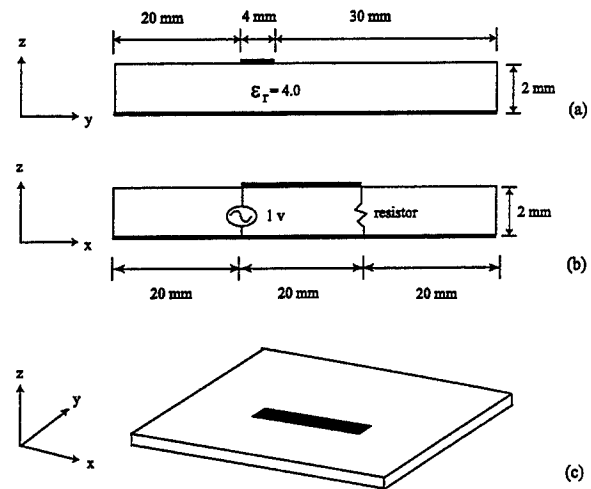


Figure 6. A microstrip geometry. (a) y-z plane view, (b) x-z plane view, and (c) 3D view.

Table 1. Impedances obtained using EMAP5.

Source Frequency (MHz)	$(Z_{in})_{open}$ (Ohms)	$(Z_{in})_{short}$ (Ohms)	Z_0 (Ohms)
300	-j187	+j17	56.4
500	-j106	+j30	56.4
700	-j69	+j46	56.3

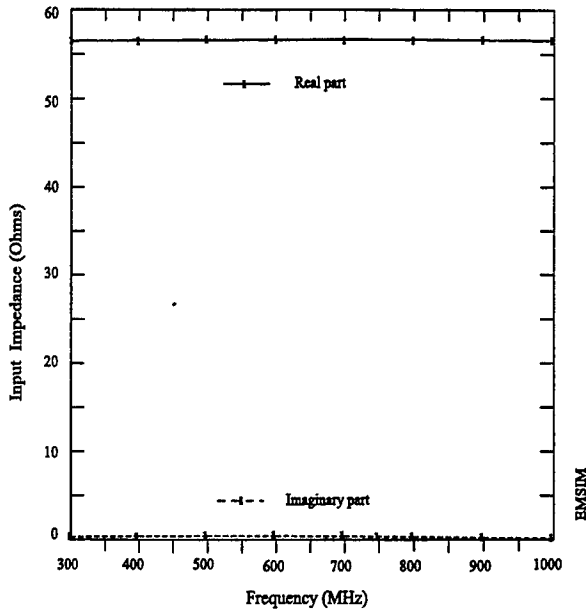


Figure 7. The input impedance obtained using EMSIM with a 56-Ohm load resistor.

The third example simulates the coupling between an active trace and an off-board trace on a printed circuit board. As shown in Figure 8, the active trace is excited by a 1-volt, 600 MHz source at one end, and is terminated by a 50-Ohm resistor at the other end. The off-board trace runs parallel to the active trace and extends well off the board. In EMAP5's hybrid solution, the dielectric volume is divided into 900 tetrahedra. The surface is divided into 876 triangles. For the first test case, there is no dielectric material between the traces and the ground. Therefore, the model contains only perfect electrical conductor (PEC) and can be analyzed using only the MoM portion of EMAP5. Figure 9 shows the current on the off-board trace obtained by EMAP5 compared with results obtained by EMSIM. For the second test case, the dielectric constant of the slab is set to 4.0. Figure 10 shows the results obtained by EMAP5 compared with results obtained using EMSIM. For both cases, good agreement is obtained between EMAP5 and EMSIM.

The fourth example models a printed circuit board power bus structure. As shown in Figure 11, the top and the bottom planes of the board are PEC. The dielectric between the top and bottom planes has a relative permittivity of 4.3(1-j0.02). Two test ports are identified at the locations shown in Figure 11. In EMAP5's hybrid solution, the dielectric volume is divided into 1,500 tetrahedra. The surface of the dielectric and the metal plates are divided into 1,340 triangle patches. The model is verified using measurements of an actual printed circuit board with the dimensions shown in Figure 11. Two 85-mil semi-

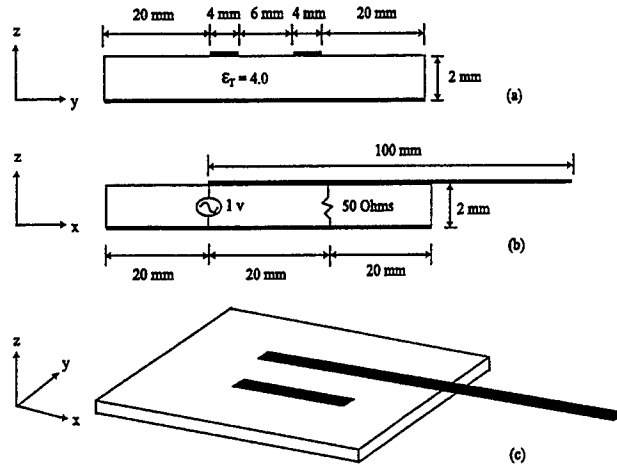


Figure 8. A grounded printed circuit board with active and passive traces. (a) y-z plane view, (b) x-z plane view, and (c) 3D view.

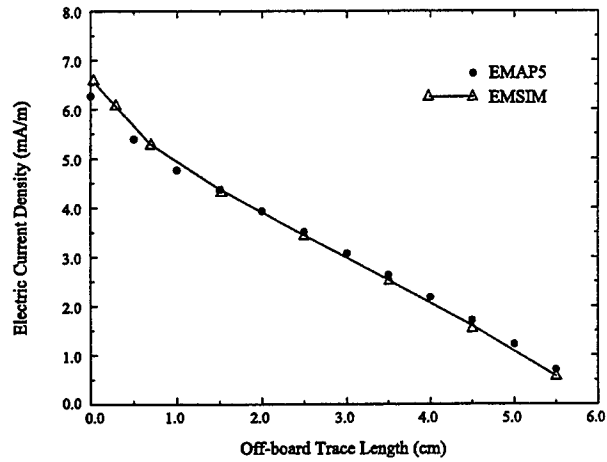


Figure 9. Current distribution on the off-board trace ($\epsilon_r = 1.0$).

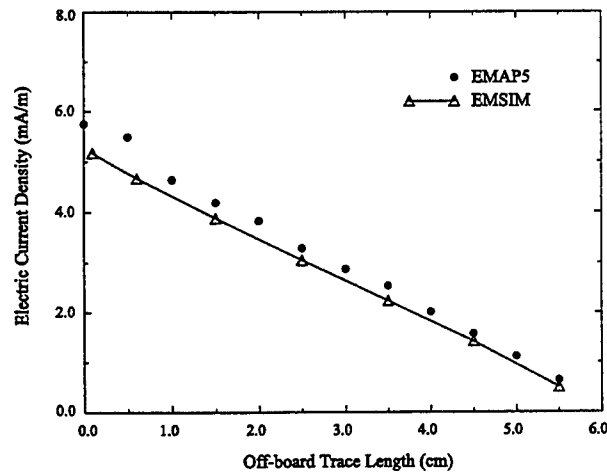


Figure 10. Current distribution on the off-board trace ($\epsilon_r = 4.0$).

rigid coaxial probes are attached at the port locations. A network analyzer is used to measure the scattering parameters of the two-port system up to 2.0 GHz. The measured and modeled $|S_{11}|$ and $|S_{21}|$ results are plotted in Figure 12 and Figure 13, respectively.

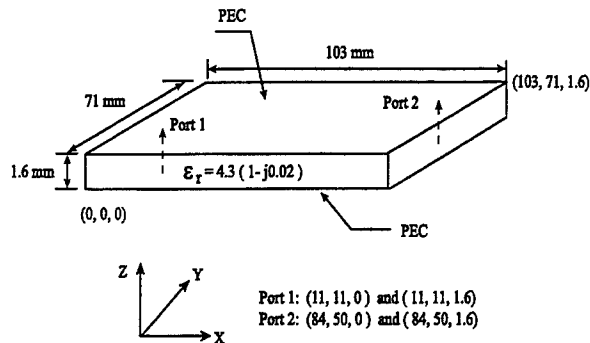


Figure 11. A two-port power bus structure.

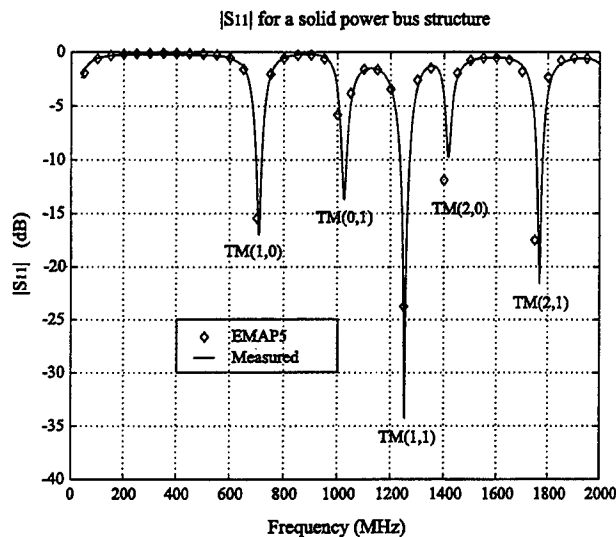


Figure 12. The measured and calculated $|S_{11}|$ for the power bus structure.

The power bus structure can be analyzed as a cavity with two PEC and four perfect magnetic conductor (PMC) walls. The cutoff frequencies are given as follows (for lossless case and $\mu_r = 1.0$) [22],

$$f_c = \frac{c}{2\pi\sqrt{\epsilon_r}} \sqrt{\left(\frac{m\pi}{a}\right)^2 + \left(\frac{n\pi}{b}\right)^2} \quad m, n = 0, 1, 2, \dots \quad (54)$$

where a and b are the length and width of the cavity, respectively; m and n are the mode indices; c is the light speed in free space; ϵ_r is the relative permittivity of the material in the cavity. For this power bus structure, only TM_z modes are excited.

Table 2 lists the calculated cutoff frequencies of the first five TM_z modes. As shown in Figure 12, the $|S_{11}|$ response dips at these resonant frequencies. At resonance, more power is delivered to the board hence more power is transmitted to Port 2 as shown in Figure 13. The measurements, numerical results and theoretical analysis agree very well.

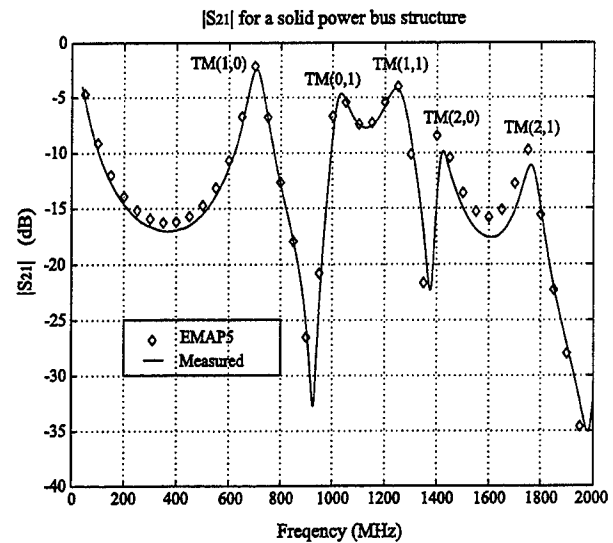


Figure 13. The measured and calculated $|S_{21}|$ for the power bus structure.

Table 2. The TM_z mode cutoff frequencies of the power bus structure.

Mode	TM_z (1,0)	TM_z (0,1)	TM_z (1,1)	TM_z (2,0)	TM_z (2,1)
fc (GHz)	0.702	1.019	1.237	1.405	1.735

VIII. SUMMARY

The EMAP5 hybrid FEM/MoM code allows users to analyze geometries with large PEC surfaces and lossy dielectrics. Unlike codes that simply use the MoM surface as an absorbing boundary for the FEM region, EMAP5 can model PEC surfaces inside, outside and adjacent to the boundary between FEM and MoM regions. This permits a variety of interesting geometries to be modeled efficiently. The SIFT5 input translation code allows users to input simple 3D geometries to EMAP5 without a graphical user interface. Four sample geometries were analyzed that demonstrate the types of problems that can be analyzed

using SIFT5 and EMAP5. Good agreement was achieved between EMAP5 results and other well-established codes, analytical results, and measurements.

REFERENCES

- [1] R. F. Harrington, *Field Computation by Moment Methods*, pp. 1-9, New York: Macmillan, 1968.
- [2] D. G. Dudley, *Mathematical Foundations for Electromagnetic Theory*, pp. 33-36, New York: IEEE Press and Oxford University Press, 1994.
- [3] X. Yuan, D. R. Lynch, and J. W. Strohbehm, "Three-dimensional finite, boundary, and hybrid element solutions of the Maxwell's equations for lossy dielectric media," *IEEE Trans. on Microwave Theory and Tech.*, vol. 36, pp. 682-693, Apr. 1988.
- [4] J.-M. Jin and J. L. Volakis, "Electromagnetic scattering by and transmission through a three-dimensional slot in a thick conducting plane," *IEEE Trans. on Antennas and Propagat.*, vol. 39, pp. 543-550, Apr. 1991.
- [5] A. J. Sangster and H. Wang, "A combined FEM/MoM technique of coupling radiating apertures in rectangular waveguide," *IEEE Trans. on Magnetics*, vol. 31, pp. 1554-1557, May 1995.
- [6] M. W. Ali, T. H. Hubing, and J. L. Drewniak, "A hybrid FEM/MoM technique for electromagnetic scattering and radiation from dielectric objects with attached wires," *IEEE Trans. on Electromagnetic Compatibility*, vol. 39, pp. 304-314, Nov. 1997.
- [7] M. W. Ali, "Development of a hybrid 3D numerical modeling technique for analyzing printed circuit models with attached wires," Ph.D. dissertation, University of Missouri-Rolla, Dec. 1996.
- [8] A. F. Peterson, S. L. Ray, and R. Mittra, *Computational Methods for Electromagnetics*, pp. 461-463, New York: IEEE Press and Oxford University Press, 1997.
- [9] P. P. Silvester and R. L. Ferrari, *Finite Elements for Electrical Engineers*, 3rd edition, pp. 405-406 New York: Cambridge University Press, 1996.
- [10] J. L. Volakis, A. Chatterjee, and L. C. Kempel, *Finite Element Method for Electromagnetics*, New York: IEEE Press and Oxford University Press, 1998.
- [11] J.-M. Jin, *The Finite Element Method in Electromagnetics*, New York: John Wiley & Sons Inc, 1993.
- [12] M. L. Barton and Z. J. Cendes, "New vector finite elements for three-dimensional magnetic field computation," *Journal of Applied Physics*, vol. 61, pp. 3919-3921, Apr. 1987.
- [13] J. J. H. Wang, *Generalized Moment of Methods in Electromagnetics*, pp. 171-174, New York: John Wiley & Sons, 1990.
- [14] S. M. Rao, D. R. Wilton, and A. W. Glisson, "Electromagnetic scattering by surfaces of arbitrary shape," *IEEE Trans. on Antennas and Propagat.*, vol. 30, pp. 409-418, May 1982.
- [15] C. A. Balanis, *Advanced Engineering Electromagnetics*, 2nd edition, pp. 285-288, New York: John Wiley & Sons, 1989.
- [16] D. A. H. Jacobs, "A generalization of the conjugate gradient method to solve complex systems," *IMA J. Numerical Anal.*, vol. 6, pp. 447-452, 1986.
- [17] W. H. Press, S. A. Teukolsky, W. T. Vetterling, and B. P. Flannery, *Numerical Recipes in C: The Art of Scientific Computing*, 2nd edition, New York: Cambridge University Press, 1992.
- [18] T. H. Hubing, H-H. Lim, and J. L. Drewniak, "A geometry description language for 3D electromagnetic analysis codes," *Proceedings of the 10th Annual Review of Progress in Applied Computational Electromagnetics*, pp. 417-422, Mar. 1994.
- [19] Y. Ji, "Enhancements to EMAP5", M.S. thesis, University of Missouri-Rolla, Dec. 1997.
- [20] EMAP5 web page at <http://www.emclab.UMR.edu/emap5>.
- [21] E. Arvas, A. Rahhal-Arabi, and A. Sadigh, "Scattering from multiple conducting and dielectric bodies of arbitrary shape," *IEEE Antenna and Propagation Magazine*, vol. 33, No. 2, Apr. 1991.
- [22] D. M. Pozar, *Microwave Engineering*, 2nd edition, New York: John Wiley & Sons Inc, 1998.
- [23] EMSIM is a 3D numerical electromagnetic modeling code marketed by Pacific Numerix, Scottsdale, AZ, <http://www.pnc.com>.

Appendix A. Evaluation of B Matrix

The elements in B are given by,

$$B_{mn} = \int_{S_m} \mathbf{w}_m(\mathbf{r}) \cdot \mathbf{f}_n(\mathbf{r}) dS. \quad (\text{A-1})$$

When edge m and n do not lie on a common triangle, B_{mn} is zero. In addition, $B_{mn} = 0$ when $m=n$, because

$$\mathbf{w}_n(\mathbf{r}) = \hat{\mathbf{n}} \times \mathbf{f}_n(\mathbf{r}). \quad (\text{A-2})$$

If edge m and n lie on a common triangle T^q , B_{mn} is given by,

$$\begin{aligned} B_{mn} &= \int_{S_m} \mathbf{w}_m(\mathbf{r}) \cdot \mathbf{f}_n(\mathbf{r}) dS = \int_{S_m} [\hat{\mathbf{n}} \times \mathbf{f}_m(\mathbf{r})] \cdot \mathbf{f}_n(\mathbf{r}) dS \\ &= \int_{S_m} \hat{\mathbf{n}} \cdot [\mathbf{f}_m(\mathbf{r}) \times \mathbf{f}_n(\mathbf{r})] dS = \hat{\mathbf{n}} \cdot \int_{S_m} [\mathbf{f}_m(\mathbf{r}) \times \mathbf{f}_n(\mathbf{r})] dS \\ &= \left(\frac{\pm l_m}{2A^q} \right) \left(\frac{\pm l_n}{2A^q} \right) \hat{\mathbf{n}} \cdot \int_{S_m} [(\mathbf{r} - \mathbf{r}_m) \times (\mathbf{r} - \mathbf{r}_n)] dS \\ &= \left(\frac{\pm l_m}{2A^q} \right) \left(\frac{\pm l_n}{2A^q} \right) \hat{\mathbf{n}} \cdot \int_{S_m} [\mathbf{r}_m \times \mathbf{r}_n + (\mathbf{r}_n - \mathbf{r}_m) \times \mathbf{r}] dS. \quad (\text{A-3}) \end{aligned}$$

The \pm signs before l_m and l_n refer to the edge directions of edge m and edge n , respectively. The integral term in Equation (A-3) can be evaluated using the one-point Gaussian Quadrature technique,

$$B_{mn} = \frac{(\pm l_m)(\pm l_n)}{4A^q} \hat{\mathbf{n}} \cdot [\mathbf{r}_m \times \mathbf{r}_n + (\mathbf{r}_n - \mathbf{r}_m) \times \mathbf{r}^{\text{cp}}] \quad (\text{A-4})$$

where \mathbf{r}^{cp} is the centroid of triangle T^q .

Appendix B. Evaluation of Matrix D

The elements in matrix D are given by,

$$\begin{aligned} D_{mn} &= \int_{S_m} \mathbf{f}_m(\mathbf{r}) \cdot \left[\int_{S_n} \mathbf{f}_n(\mathbf{r}') \times \nabla' G_0(\mathbf{r}, \mathbf{r}') dS' + \frac{1}{2} \mathbf{w}_n(\mathbf{r}) \right] dS \\ &= -\frac{1}{2} B_{mn} + D'_{mn} \quad (\text{since } B_{mn} = -B_{nm}) \quad (\text{B-1}) \end{aligned}$$

where D'_{mn} is defined as follows,

$$\begin{aligned} D'_{mn} &= \int_{S_m} \mathbf{f}_m(\mathbf{r}) \cdot \left[\int_{S_n} \mathbf{f}_n(\mathbf{r}') \times \nabla' G_0(\mathbf{r}, \mathbf{r}') dS' \right] dS \\ &= \left(\frac{\pm l_m}{2A^m} \right) \left(\frac{\pm l_n}{2A^n} \right) \int_{S_m} (\mathbf{r} - \mathbf{r}_m) \\ &\quad \cdot \left[\int_{S_n} (\mathbf{r}' - \mathbf{r}'_n) \times \nabla' G_0(\mathbf{r}, \mathbf{r}') dS' \right] dS \end{aligned} \quad (\text{B-2})$$

$$\nabla' G_0(\mathbf{r}, \mathbf{r}') = \frac{1 + j k_0 R}{4\pi R^3} e^{-j k_0 R} \mathbf{R} \quad (\text{B-3})$$

where $\mathbf{R} = \mathbf{r} - \mathbf{r}'$, $R = |\mathbf{R}|$. The \pm signs before l_m and l_n refer to the edge directions of edge m and edge n , respectively. Because the EFIE given by Equation (8) already excludes the singularity at $\mathbf{r} = \mathbf{r}'$, D'_{mn} can be evaluated directly using the seven-point Gaussian Quadrature technique.

A Hybrid MoM/FEM Technique for Scattering from a Complex BOR with Appendages

Andrew D. Greenwood
Air Force Research Laboratory
Directed Energy Directorate
Kirtland AFB, NM 87117

Jian-Ming Jin
ECE Department
University of Illinois
Urbana, IL 61801

Abstract

A hybrid technique is developed to allow the scattering from small appendages to be approximately combined with the scattering from a large body of revolution (BOR). The hybrid technique thus enables the rotational symmetry of the large BOR to be exploited to solve the scattering problem with much less computational complexity than a fully three-dimensional (3-D) solution. The technique combines the finite element method (FEM) for BOR scattering with the method of moments (MoM) for small appendages. The hybrid formulation is discussed in detail, including an approximate Green's function which permits the decoupling of the solutions from the FEM and the MoM. Numerical examples are given to show the applicability and accuracy of the hybrid technique.

1 Introduction

The symmetry present in body of revolution (BOR) electromagnetic scattering problems permits an efficient numerical solution using a two-dimensional (2-D) technique [1]–[5]. However, in many practical problems, the rotational symmetry is broken by the presence of small appendages (see Fig. 1). Thus, a three-dimensional (3-D) computational method is required to rigorously compute the electromagnetic scattering. Because of the increased computational complexity of a 3-D method, a hybrid method is developed to allow the scattering from small appendages to be approximately combined with the scattering from a large BOR in a manner similar to other hybrid techniques [6]–[9]. The rotational symmetry can then be exploited in the computation of the scattering from the large BOR. The hybrid method makes use of the finite element method (FEM) for BOR scattering as described in [4], and the method of moments (MoM) for small appendages as described in [8]. The remainder of this paper discusses the hybridization of the two methods. The formulation is presented in Section 2, numerical results are given in Section 3, and concluding remarks are found in Section 4.

2 Formulation

As mentioned, the two methods to be hybridized are the FEM for BOR scattering and the MoM for small appendages. The FEM for BOR scattering makes use of edge-based vector basis functions to expand the transverse field components and node-based scalar basis functions to expand the angular component. This mixed edge-node formulation eliminates the problem of spurious modes [4], and it directly computes all components of the electric field. The coupled azimuth potential formulation, which computes the angular component of the electric and magnetic fields, is less accurate than the mixed edge-node formulation [5]. Mesh truncation for the FEM is accomplished using cylindrical perfectly matched layer (PML), which is efficient and accurate. PML does not alter the sparsity of the FEM matrix, and it avoids the wasted computation required by a spherical mesh boundary for an elongated geometry. Finally, the FEM equations are solved using band matrix decomposition techniques. Validation examples showing the efficiency and accuracy of the method are found in [4].

The MoM used with the hybrid method is straightforward and makes use of the well-known Rao-Wilton-Glisson (RWG) basis functions. The MoM matrix equations encountered are typically of low dimension and are thus solved using simple LU-decomposition techniques. If necessary, fast multipole techniques can be employed for larger problems [10].

The hybrid formulation is best understood by first considering the computation of the scattering from a BOR with appendages (see Fig. 1) entirely by the MoM. Assuming that the entire target consists of perfect conductors, the application of the MoM uses the integral equation

$$\mathbf{E}(\mathbf{r}) = \mathbf{E}^i(\mathbf{r}) - jk_0\eta_0 \iint_S \mathbf{G}_0(\mathbf{r}, \mathbf{r}') \cdot \mathbf{J}(\mathbf{r}') dS' \quad (1)$$

where $k_0 = \omega\sqrt{\mu_0\epsilon_0}$ is the free-space wavenumber, $\eta_0 = \sqrt{\mu_0/\epsilon_0}$ is the impedance of free space, \mathbf{G}_0 is the free-space dyadic Green's function, \mathbf{E}^i is a known incident electric field, \mathbf{J} is the unknown current on the surface of the target, and S is the surface of the entire target. When using the MoM, \mathbf{J}

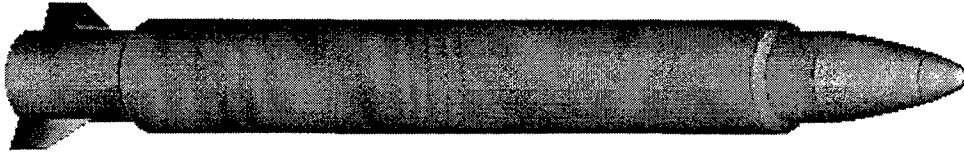


Figure 1: Example of a large BOR with small appendages.

is found by discretizing the surface S and applying the appropriate boundary condition on the discretized surface. The scattered field is then found from

$$\mathbf{E}^s(\mathbf{r}) = -jk_0\eta_0 \iint_S \mathbf{G}_0(\mathbf{r}, \mathbf{r}') \cdot \mathbf{J}(\mathbf{r}') dS'. \quad (2)$$

This 3-D method generates a dense matrix equation; therefore, if the geometry is large, the method is computationally very intensive. Further, if the BOR contains inhomogeneous materials, the surface integral in Eq. (1) must be replaced with a volume integral, further increasing the computational complexity.

Because of the unfavorable computational complexity in solving Eq. (1) with the MoM, an alternate, hybrid method is sought. In the hybrid method, the MoM is applied to the small appendages only. Thus, Eq. (1) becomes

$$\mathbf{E}(\mathbf{r}) = \mathbf{E}_{\text{BOR}}^i(\mathbf{r}) - jk_0\eta_0 \iint_{S_{\text{App}}} \mathbf{G}_{\text{BOR}}(\mathbf{r}, \mathbf{r}') \cdot \mathbf{J}(\mathbf{r}') dS' \quad (3)$$

where $\mathbf{E}_{\text{BOR}}^i$ represents the incident field on the appendages in the presence of the BOR, S_{App} represents the surface of the appendages, and \mathbf{G}_{BOR} represents the dyadic Green's function in the presence of the BOR. The solution of Eq. (3) requires the discretization of S_{App} rather than S and thus is much less computationally intensive. The incident field $\mathbf{E}_{\text{BOR}}^i$ is calculated using the FEM [4], but difficulty is still encountered in solving Eq. (3) with the MoM because the Green's function \mathbf{G}_{BOR} is, in general, unknown. The unknown Green's function is needed not only for the solution of Eq. (3), but also to compute the scattered electric field from

$$\mathbf{E}^s(\mathbf{r}) = -jk_0\eta_0 \iint_{S_{\text{App}}} \mathbf{G}_{\text{BOR}}(\mathbf{r}, \mathbf{r}') \cdot \mathbf{J}(\mathbf{r}') dS'. \quad (4)$$

The difficulty posed by the unknown Green's function \mathbf{G}_{BOR} is alleviated in two ways. An approximate Green's function is used for the solution of Eq. (3), and an alternate method based on the reciprocity theorem is used to compute \mathbf{E}^s .

There are four steps to using the hybrid method. First, the FEM described in [4] is used to compute scattering from the large BOR alone. Then, the result of the first step is used to compute $\mathbf{E}_{\text{BOR}}^i$, the incident field on the appendages in the presence of the BOR. Next, the MoM with an approximate Green's function is used to solve Eq. (3) for \mathbf{J} , the current on the appendages. Note that in the usual MoM analysis with RWG basis functions, the unknowns are placed on

edges which are shared by two facets in the mesh. In the hybrid method, unknowns must also be placed on the boundary edges connecting the appendages to the large BOR to account for current flow from the appendages to the large BOR [8]. Finally, the scattered field generated by \mathbf{J} is evaluated using reciprocity and added to the scattered field from the BOR, which is found in the first step. The result is an approximation to the scattered field from the entire structure. In the remainder of this section, the construction of the approximate Green's function and the computation of the scattered field by reciprocity are each discussed in turn.

2.1 Approximate Green's function

The approximate Green's function used to solve Eq. (3) is developed by approximating the BOR on which the appendages reside as a long cylinder. The approximate Green's function must model the significant field interactions between points on the appendages but may neglect other, less significant interactions. The interactions are classified into four types. The first type of interaction is the direct path interaction between two points, and examples of this type of interaction are illustrated in Fig. 2a. The second type of interaction involves a reflection by the large BOR, and examples are illustrated in Fig. 2b. The third interaction type is the surface wave interaction which is illustrated in Fig. 2c. All other interactions are classified as the fourth type. Most of these are complex interactions which are not modeled by the cylinder approximation to the BOR, and most are negligible.

If the line of sight between two points on the appendages is unobstructed by the cylinder approximation to the large BOR, the first two interaction types can be computed using the half-space Green's function. This is done by finding the reflection point on the cylinder and computing the tangent plane to the cylinder at that point. If the line of sight between the two appendage points is obstructed by the cylinder, both of the first two interactions are zero. For many problems, modeling the first two interactions produces acceptable results. If better accuracy is desired, the third type of interaction can be computed using the geometrical theory of diffraction (GTD) [11]. Also, if the appendages are near the end of the BOR, it may be necessary to compute an interaction based on edge diffraction from the nearby end. Note that the effect of neglecting some of the interactions is to neglect the

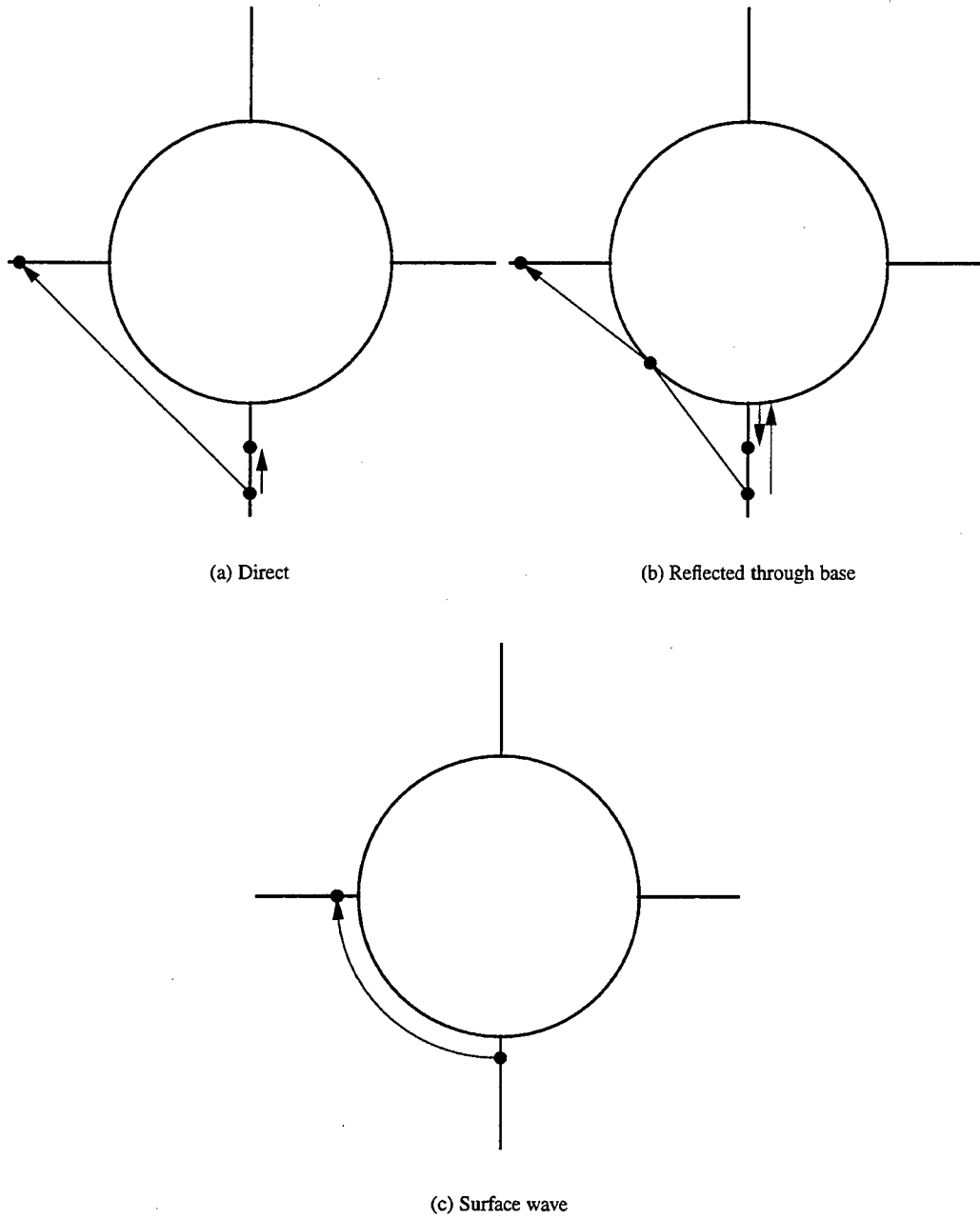


Figure 2: Interactions between appendage points.

corresponding field which is scattered by the appendages, reflected or diffracted back to the appendages, and scattered by the appendages again [6]–[9].

In all of the examples presented in this paper, the approximate Green's function models the first two interaction types (Fig. 2a-b) and neglects all other interactions. To compute values of the approximate Green's function, the geometry of the protrusions is first examined, and the radius of the infinite cylinder used to approximate the large BOR is found from the points where the protrusions attach to the BOR. Given any two points on the protrusions, the value of the Green's function is then computed in a four step process. First, the direct (line of sight) path between the two points is computed. If this path is blocked by the infinite cylinder, there is no line of sight interaction. Next, the interaction involving a reflection by the infinite cylinder is considered. The reflection point is found using Snell's law. Note that it can be shown that if there is no direct interaction, there is also no reflected interaction. Thus, if there is no direct path, the value of the approximate Green's function between the two points is zero. If there is a direct path, the third step is the application of a coordinate translation and rotation such that in the transformed space, the reflection point is on the $z = 0$ plane and the normal to the cylinder at the reflection point is in the \hat{z} direction. Finally, the half-space Green's function is applied in the transformed space to compute the value of the approximate Green's function between the two given points.

2.2 Computation of scattered field

While the use of the approximate Green's function allows Eq. (3) to be solved for \mathbf{J} , the approximation is not accurate when computing \mathbf{E}^s from Eq. (4). Therefore, an alternate method of computing \mathbf{E}^s is used. The alternate method is based on the reciprocity theorem. Consider a short dipole, located at point \mathbf{r} and oriented in the \hat{u} direction. From the reciprocity theorem,

$$\mathbf{E}^s(\mathbf{r}) \cdot \hat{u} = -jk_0\eta_0 \frac{e^{-jk_0r}}{4\pi r} \iint_{S_{App}} \mathbf{E}_{BOR}^r(\mathbf{r}') \cdot \mathbf{J}(\mathbf{r}') dS' \quad (5)$$

where \mathbf{E}_{BOR}^r is the field radiated by the dipole in the presence of the large BOR. Recall that this field can be computed by the FEM. In fact, when backscattering is being computed, \mathbf{E}_{BOR}^r is the same as \mathbf{E}_{BOR}^i that is used in Eq. (3). Thus, all components needed to compute \mathbf{E}^s using Eq. (5) are known.

3 Numerical Results

Several numerical results are presented to show the validity and capability of the hybrid technique. In all of the results presented, the direct and reflected interactions are modeled by the approximate Green's function, and all other interactions are neglected.

First, the validity of the technique is tested by computing the scattering from metallic cylinders with capped ends and one, two, or four wings. The scattering is compared with computations from the Fast Illinois Solver Code (FISC) [10], which is an MoM program that uses a multilevel fast multipole algorithm to speed up the matrix solution. The cylinders considered have a radius of 1.25λ and height of 5λ , where λ is the free-space electromagnetic wavelength. The cap at one end of the cylinder is pointed, while the cap at the other end is rounded. The attached wings are 1λ by 0.5λ by 0.025λ .

The monostatic RCS as a function of azimuth angle from the capped cylinder with one wing is shown in Fig. 3. The agreement between FISC and the hybrid method is very good. The scattering from the cylinder without the wing is flat as a function of azimuth angle, so it can be seen that the wing has added approximately 5 dB peak-to-peak swing to the RCS in the VV-polarized case and about 4 dB peak-to-peak swing in the HH-polarized case. Although adding a second wing presents the possibility of more complex interactions, the results shown in Fig. 4 continue to show good agreement between FISC and the hybrid method. The peak-to-peak variation in the RCS is about 4.5 dB in the VV-polarized case and almost 6 dB in the HH-polarized case when two wings are present. The scattering from the cylinder with four wings is shown in Fig. 5, where the agreement between FISC and the hybrid method remains very good. With four wings present, the peak-to-peak swing in the RCS is about 5 dB in the VV-polarized case and about 6 dB in the HH-polarized case.

To further illustrate the capability of the hybrid method, two more computed results are presented. Both of these results involve 1-GHz scattering from a missile with appendages. The missile is 12.5 m (41.7 λ) long and has a radius of 0.625 m (2.1 λ). For the first case, a 3-cm (0.1 λ) by 3-cm (0.1 λ) by 8.125-m (27.7 λ) ridge is located on the missile at azimuth angle 0° , and computed results for an azimuth scan and for an elevation scan are presented in Fig. 6. Note that in the azimuth scan, the ridge causes the scattering to vary over a 3.5-dB range in the VV-polarized case and over a 3-dB range in the HH-polarized case while the missile alone, because of its rotational symmetry, has a constant RCS as a function of azimuth angle. In the second case, two fins are located on the missile at azimuth angles 90° and -90° . The fins are trapezoidal in shape with a height of 0.375 m (1.25 λ), bases of 1 m (3.33 λ) and 0.5 m (1.67 λ), and a thickness of 0.01 m (0.03 λ). The scattering is shown both for an azimuth cut and for an elevation cut in Fig. 7. In the azimuth cut, the scattering has changed from flat for the missile alone to a function with a 3 dB peak-to-peak variation in the VV-polarized case and a 2 dB peak-to-peak variation in the HH-polarized case.

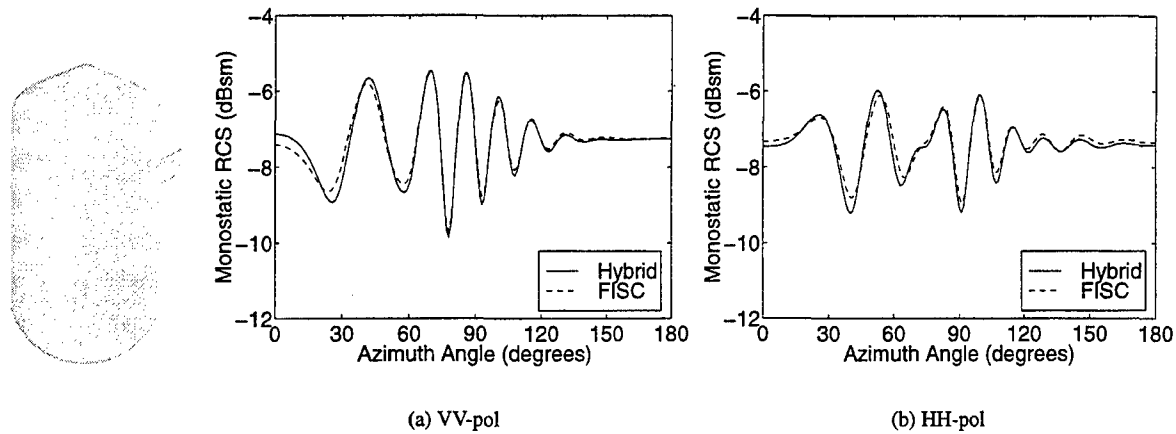


Figure 3: RCS of a metallic capped cylinder with a wing. The cylinder has a radius of 1.25λ and height of 5λ , and the wing is 1λ by 0.5λ by 0.025λ .

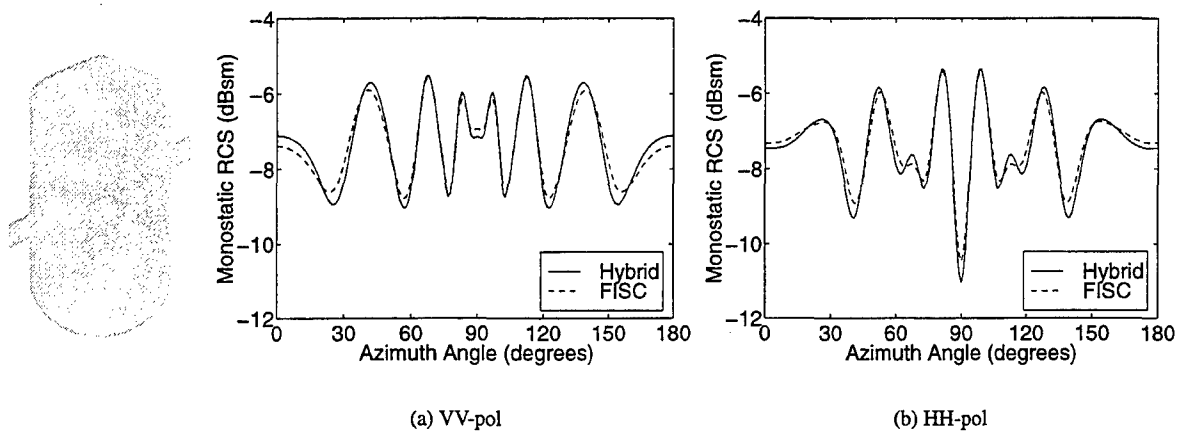


Figure 4: RCS of a metallic capped cylinder with two wings. The cylinder has a radius of 1.25λ and height of 5λ , and the wings are 1λ by 0.5λ by 0.025λ .

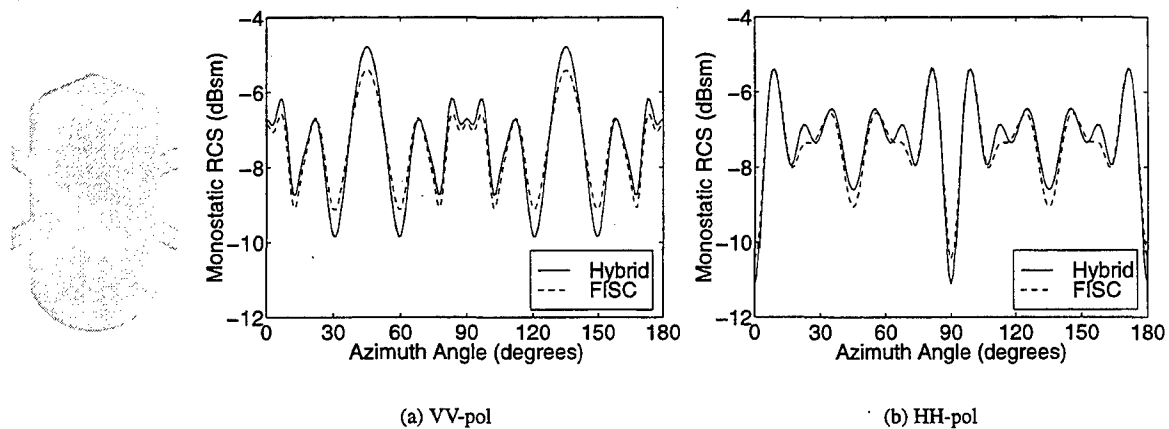


Figure 5: RCS of a metallic capped cylinder with four wings. The cylinder has a radius of 1.25λ and height of 5λ , and the wings are 1λ by 0.5λ by 0.025λ .

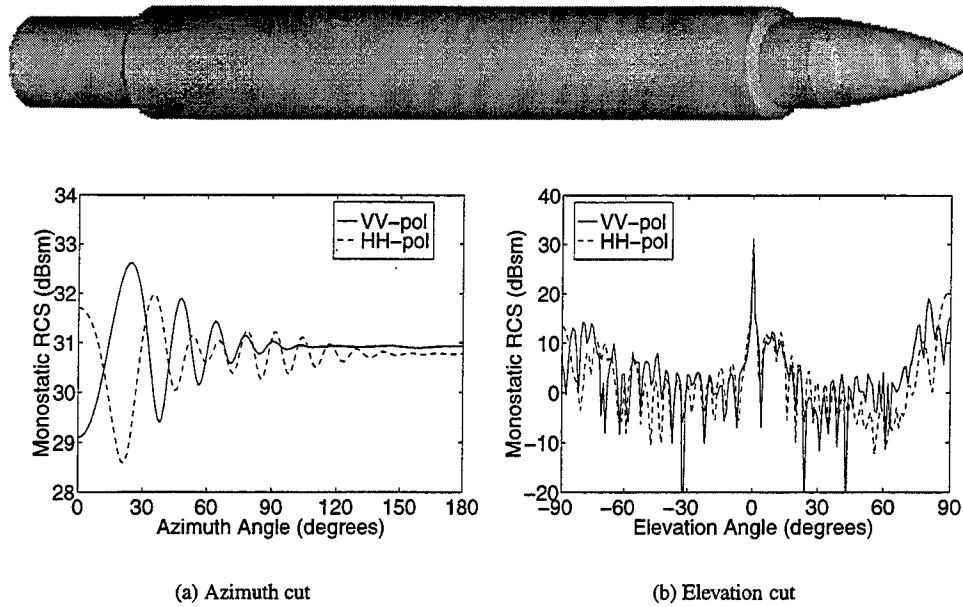


Figure 6: RCS of a missile with a ridge at 1 GHz. The missile is 12.5 m (41.7λ) long and has a radius of 0.625 m (2.1λ). The ridge is 3 cm (0.1λ) by 3 cm (0.1λ) by 8.125 m (27.7λ) and located at azimuth angle 0° .

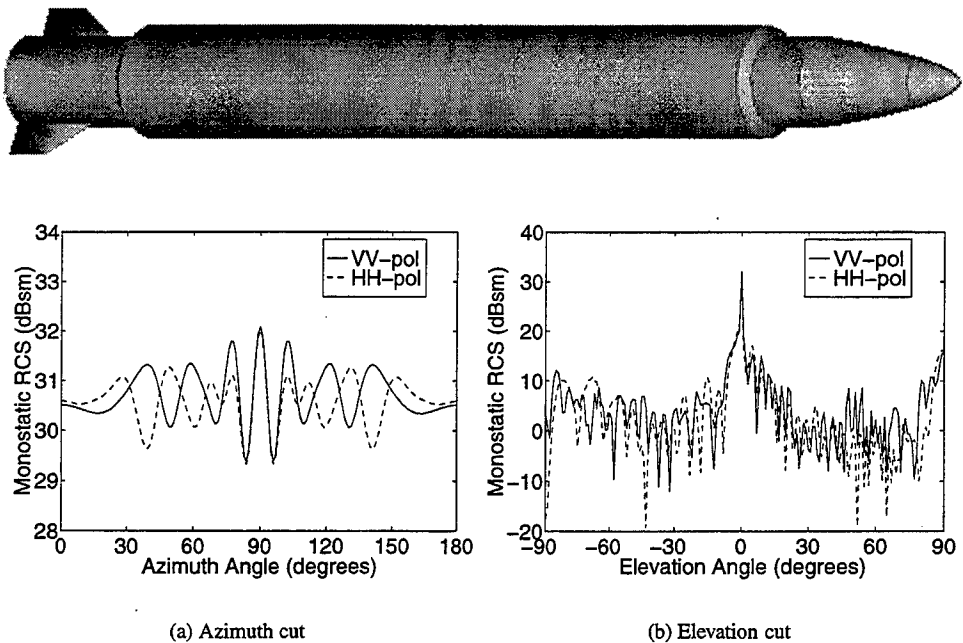


Figure 7: RCS of a missile with two fins at 1 GHz. The missile is 12.5 m (41.7λ) long and has a radius of 0.625 m (2.1λ). The fins are trapezoidal with a height of 0.375 m (1.25λ), bases of 1 m (3.33λ) and 0.5 m (1.67λ), and a thickness of 0.01 m (0.03λ); they are located at azimuth angles 90° and -90° .

4 Summary

The hybrid method is a useful extension of the FEM/BOR capability described in [4]. While rigorous computation of scattering from a BOR with appendages requires a 3-D computational method, the hybrid method separates the BOR part of the problem from the appendages. The rotational symmetry of the BOR part of the problem can then be exploited for computational efficiency while only the appendage part, which is typically much smaller than the BOR part, requires a 3-D method. Numerical results show the impact of the appendages on the scattering from the entire structure and verify the validity and capability of the hybrid method.

References

- [1] M. G. Andreasen, "Scattering from bodies of revolution," *IEEE Trans. Antennas Propagat.*, vol. 13, pp. 303–310, 1965.
- [2] J. R. Mautz and R. F. Harrington, "Electromagnetic scattering from a homogeneous material body of revolution," *Arch. Elektron. Uebertragungstechn.*, vol. 33, pp. 71–80, 1979.
- [3] L. N. Medgyesi-Mitschang and J. M. Putnam, "Electromagnetic scattering from axially inhomogeneous bodies of revolution," *IEEE Trans. Antennas Propagat.*, vol. 32, pp. 797–806, 1984.
- [4] A. D. Greenwood and J. M. Jin, "A novel efficient algorithm for scattering from a complex BOR using mixed finite elements and cylindrical PML," *IEEE Trans. Antennas Propagat.*, vol. 47, pp. 620–629, 1999.
- [5] A. D. Greenwood and J. M. Jin, "Computation of the RCS of a complex BOR using FEM with coupled azimuth potentials and PML," *Electromagn.*, vol. 19, pp. 147–170, 1999.
- [6] J. M. Jin, S. S. Ni, and S. W. Lee, "Hybridization of SBR and FEM for scattering by large bodies with cracks and cavities," *IEEE Trans. Antennas Propagat.*, vol. 43, pp. 1130–1139, 1995.
- [7] A. D. Greenwood, S. S. Ni, and J. M. Jin, "Hybrid FEM/SBR method to compute the radiation pattern from a microstrip patch antenna in a complex geometry," *Microwave Opt. Tech. Lett.*, vol. 13, pp. 84–87, 1996.
- [8] J. M. Jin, F. Ling, S. T. Carolan, J. M. Song, W. C. Gibson, and W. C. Chew, "A hybrid SBR/MoM technique for analysis of scattering from small protrusions on a large conducting body," *IEEE Trans. Antennas Propagat.*, vol. 46, pp. 1349–1357, 1998.
- [9] A. D. Greenwood and J. M. Jin, "Hybrid MoM/SBR method to compute the scattering from a slot array antenna in a complex geometry," *ACES Journal*, vol. 13, pp. 43–51, 1998.
- [10] J. M. Song, C. C. Lu, and W. C. Chew, "Multilevel fast multipole algorithm for electromagnetic scattering by large complex objects," *IEEE Trans. Antennas Propagat.*, vol. 45, pp. 1488–1493, 1997.
- [11] P. Munk, "A uniform geometrical theory of diffraction for the radiation and mutual coupling associated with antennas on a material coated convex conducting surface," Ph.D. dissertation, The Ohio State University, Columbus, OH, 1996.

IMPEDANCE OF A HALF-WAVE DIPOLE OVER A FINITE GROUND PLANE

P R Foster* and R A Burberry**

*Microwave and Antenna Systems, UK

** Consultant, UK

ABSTRACT

A study has been carried out on the impedance of a half-wave dipole above a finite ground plane. The Method of Moment code, NEC-4, has been used and it has been found that for ground planes which are greater than 1.0 by 1.0 wavelengths, the changes from the effect with an infinite plane are negligible. With very small planes, the current distribution across the ground plane and the impedance are substantially different from those with larger ground planes.

1. INTRODUCTION

There is a dearth of information in the open literature on the effect of a finite ground plane on the impedance of a nearby halfwave dipole although several authors have considered the effect of finite sheets on radiation patterns. We examine the general problem of impedance as a function of sheet size and dipole position relative to the edges of the sheet. Dipole impedances have been calculated using the Method of Moments Code, NEC-4 [1], for various dipole positions over square sheets of side 0.5, 1.0, 2.0 and 2.5λ and are examined along with theoretical considerations.

2. COMPUTATIONS

The dipole was of diameter 0.002λ (2mm) and was 0.5λ (500mm) long. Spacing from the ground plane was 0.221λ (221 mm). Throughout this paper, all dimensions are quoted in mm and in wavelengths at 300 MHz. The RF performance was examined over the frequency band 270-330 MHz.

Square sheets of size 0.5, 1.0, 2.0 and 2.5λ (500 to 2500 mm) were tested. The dipole position, initially in the centre of the sheet, was altered in steps of 0.25λ (250 mm) in either the x or y directions. The dipole lay along the x axis (Figure 1).

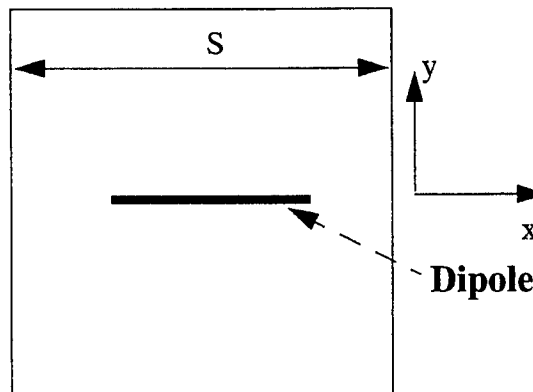


Figure 1 Geometry of Dipole over a Finite Square Ground Plane. S was varied between 0.5 and 2.5λ .

The ground planes were modelled as a square mesh with segments which were 0.05λ long (50 mm) and had a radius of 0.008λ (8.0 mm) giving a length to diameter ratio of 3.125 which is greater than the required lower limit of 2.0. This diameter is derived from the equal area rule but a convergence test was also applied (Section 7).

The dipole was modelled as 21 perfectly conducting linear segments in a length of 0.5 wavelengths (500 mm); each segment had a diameter of 0.002λ (2 mm). The excitation was a voltage source of 1 volt applied to the centre segment. Trials were carried out with 51 segments for the dipole in free space but the results were very similar to those with 21 segments (Section 7).

Computations were carried out with both double and single precision versions of NEC-4 (Section 7).

3. FREE SPACE

An initial run was made with the dipole with no ground plane present. Table 1 gives the impedance values, the resonance frequency being just below 285 MHz where the length would have been 0.473λ .

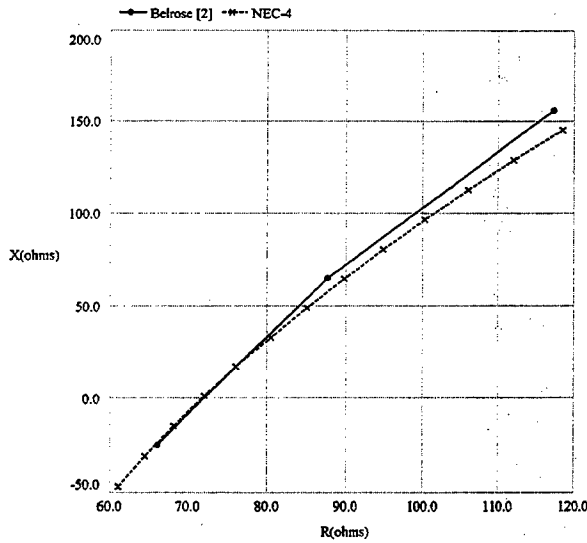


Figure 2 Reactance against Resistance for a halfwave dipole in free space The NEC-4 values are indicated at 5.0 MHz steps between 270 and 330 MHz (Table 1).

Table 1 Impedance of dipole in free space (Dipole 0.002λ diameter, 0.5λ long at 300 MHz)

F MHz	NEC-4		Belrose [2]	
	R (ohms)	X (ohms)	R (ohms)	X (ohms)
270	61.1	-46.9	66.1	-25.0
275	64.5	-30.9		
280	68.2	-14.9		
285	72.1	1.02		
290	76.1	16.9		
295	80.5	32.8		
300	85.0	48.7	87.6	65.0
305	89.8	64.6		
310	94.9	80.5		
315	100.3	96.5		
320	106.0	112.6		
325	112.1	128.7		
330	118.5	145.0	117.4	155.8

Figure 2 compares the computed impedances and those calculated from Equations 15.16 and 15.17 of Belrose, [2] which are for a monopole. These values were doubled to obtain the numbers for a dipole shown in Figure 2 and Table 1. The agreement is good. It implies that the antenna is about 3% longer electrically than its dimensions would suggest from Belrose. In their Figure 13.31, showing calculated values of resistance at resonance as a function of wavelength/diameter, Schelkunoff and Friis, [3], give a value of 64 ohms for a dipole of the dimensions used here whereas NEC-4 and Belrose both give 72 ohms.

4. GROUND PLANE

Figure 3 to Figure 5 show the impedance for the central and the two extreme positions. The values are indicated at 5.0 MHz steps between 270 and 330 MHz.

For sheets of side 1.0λ and larger, there is no significant change in impedance with sheet size when the dipole is centrally placed or when it is over a parallel edge. When the dipole is moved longitudinally so that its centre is on the edge, there is more variation with sheet size as Figure 5 demonstrates. Results for the $\lambda/2$ square sheet also show significantly lower resistance values. The impedance values for an infinite ground plane have been included in Figure 3 and show that, for plates of side greater than 1.0λ , the results have converged. For the larger sheets, there does appear to be a very slight cyclical variation with dipole position. This is shown in Table 2 for 300 MHz on a 2.5λ square sheet.

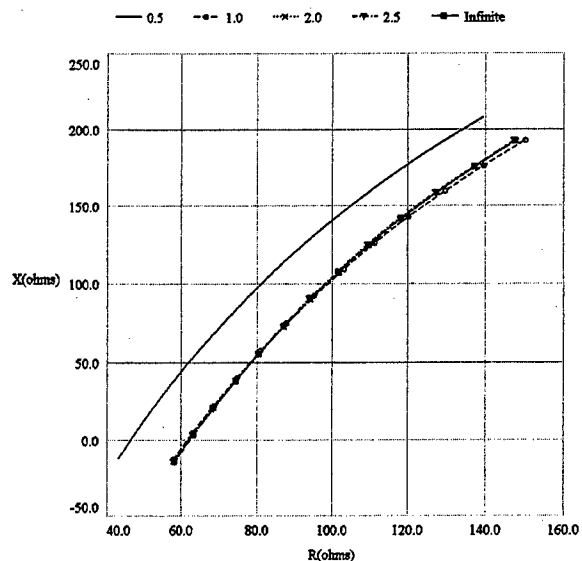


Figure 3 Impedance of dipole (Central position) between 270 and 330 MHz

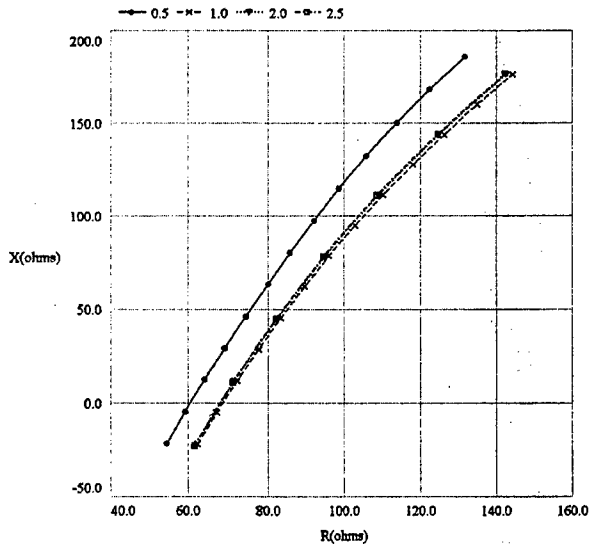


Figure 4 Impedance of dipole (over parallel edge) between 270 and 330 MHz

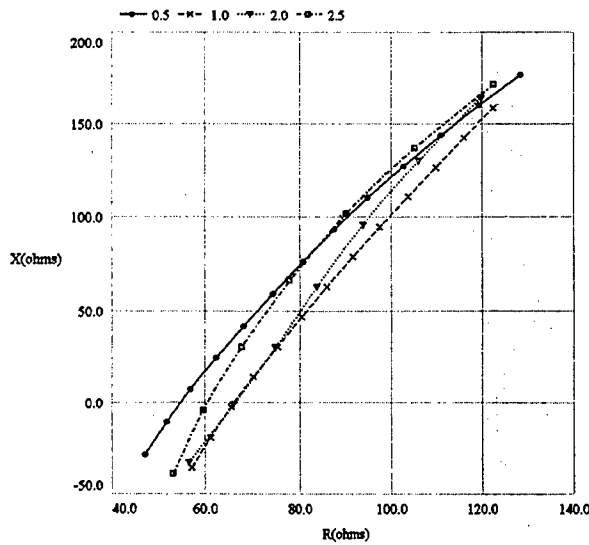


Figure 5 Impedance of dipole (over perpendicular edge) between 270 and 330 MHz.

Table 2 Impedance of dipole above ground plane of side 2.5λ as a function of position off-centre. (Frequency 300 MHz)

y/λ	$x/\lambda = 0$	x/λ	$y/\lambda = 0$
0	$93.9 + j 90.2$	0	$93.9 + j 90.2$
0.25	$94.0 + j 90.2$	0.25	$94.1 + j 90.3$
0.5	$93.9 + j 90.1$	0.5	$93.8 + j 90.0$
0.75	$94.1 + j 90.1$	0.75	$94.7 + j 90.5$
1.0	$92.6 + j 90.6$	1.0	$87.7 + j 91.6$
1.25	$94.5 + j 77.8$	1.25	$77.8 + j 66.0$

5. CURRENT FLOW

As noted above, the values of the impedance for the smallest ground plane (0.5 by 0.5λ) were quite different from those of the larger ground plane.

The currents on the ground planes at intervals of 0.25 wavelengths have been plotted for a dipole centrally placed. The abscissa (current magnitude) has been multiplied by 10^4 for convenience.

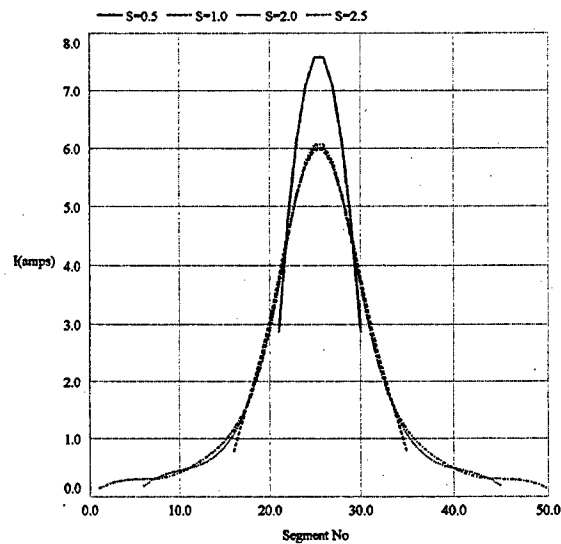


Figure 6 Current Magnitude ($\times 10^4$) on a Ground Plane parallel to the dipole and immediately below the dipole

Figure 6 shows the currents on the ground plane immediately below the dipole for several ground plane sizes while Figure 7 and Figure 8 show the currents 0.25 and

0.5 wavelength away from the centreline underneath the dipole. The most notable feature is that the current distribution is remarkably alike for ground planes with sides 1.0 to 2.5 wavelengths while the ground plane of side 0.5 wavelength is very different.

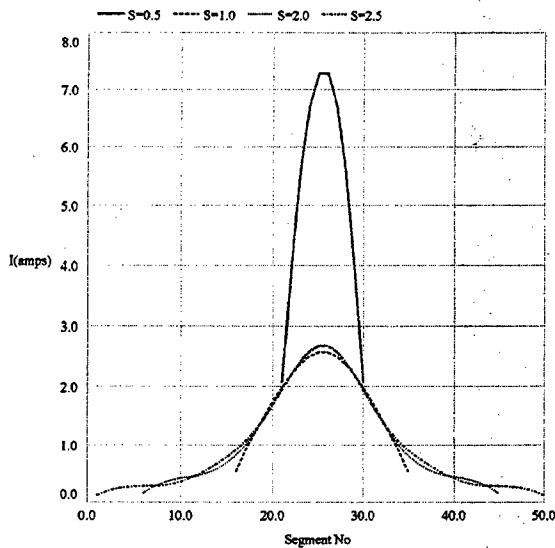


Figure 7 Current Magnitude ($\times 10^4$) on a Ground Plane parallel to the dipole and offset by 0.25 wavelength from the dipole

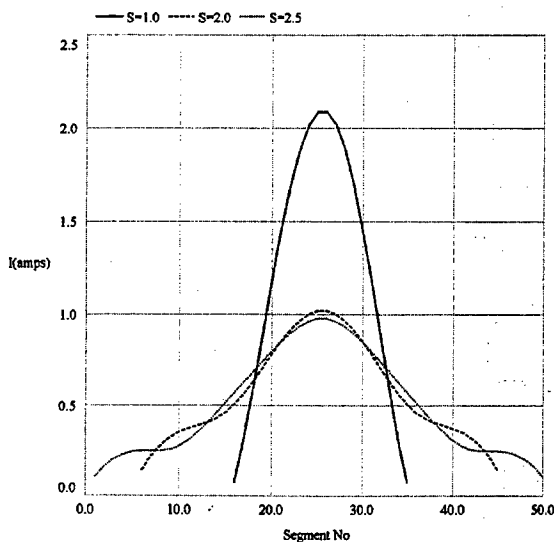


Figure 8 Current Magnitude ($\times 10^4$) on a Ground Plane parallel to the dipole and offset by 0.5 wavelengths from the dipole

6. CHECKS

It was possible to provide some corroboration for the predictions by computing the mutual impedance provided when a half-wave dipole is over an infinite ground plane. The mutual impedance is then the impedance of the dipole alone minus the mutual impedance of the dipole over an infinite ground plane. These are compared with results from Smith [5] and STC Data [4] in Table 3. These results are in better agreement with the STC data.

Since the image of the dipole in the ground plane is negative, the computed figures are in opposite senses to those from two parallel dipoles at the same spacing as the dipole and its image. The computed figures have been reversed in sign for comparison with other sets of data.

Table 3 Mutual Impedance of a Dipole above an Infinite Ground Plane

ΔF MHz	NEC-4		STC data		R A Smith	
	R	jX	R	jX	R	jX
-5.0	1.1	-31.4	1.1	-34.8	4.0	-36.9
-1.0	-1.5	-33.6	-1.5	-36.4	1.5	-36.3
+2.0	-3.7	-35.2	-3.2	-35.5	-0.3	-36.0
+4.0	-5.3	-36.2	-4.2	-35.1	-1.3	-35.7
+6.0	-7.0	-37.2	-5.2	-34.5	-2.5	-35.3
+7.0	-7.9	-37.8	-6.0	-34.1	-3.1	-35.1
RMS Error in NEC			1.2	2.6	3.8	3.0

7. CONVERGENCE TESTS

Several convergence tests were carried out on the input data.

- 1) Single and double precision versions of NEC-4 were run on all the examples for a ground plane with a side of 0.5λ . The changes in all values of impedance were less than 0.001%.
- 2) The radius of segments in the ground plane was varied between 20 and 2.5 mm with the segment length held constant at 50 mm (Figure 9). The value chosen, 8.0 mm, was based on the equal area rule and computed results agreed with other results to within 1 or 2 ohms.
- 3) The number of segments in the dipole was varied from 21 to 51. Differences of less than 1.0 degree

in phase and 1% in impedance magnitude were observed.

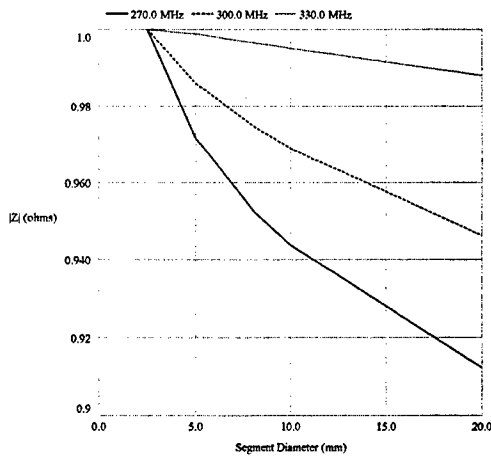


Figure 9 Impedance for three frequencies for dipole in centre of 0.5λ ground plane with the segment radii of the ground plane varied. The impedance magnitude is shown normalised to the value at a segment radius of 2.5 mm

8. CONCLUSIONS

- 1) The impedance of an isolated 0.5λ dipole obtained by NEC is closely modelled by the Belrose [2] formula for a dipole of the same dimensions. The difference of 3% in frequency may arise from small errors in Belrose's determination of electrical length which was empirical. Alternatively it may represent a genuine difference between the two models. It has been noted (Section 7) that small changes in the NEC-4 model resulted in changes in the impedance of up to 1% in magnitude.
- 2) When mounted above the centre of a finite ground plane, the dipole impedance does not alter significantly for sheets of 1λ side or larger. The resistance of a dipole above a sheet of side 0.5λ is significantly lower. The plots of current flow in Figure 6 to Figure 8 support the impedance results.
- 3) When the dipole is over the parallel edge of the sheet, the general picture is similar to that of the central position.
- 4) When the dipole centre is over the perpendicular

edge, there is more variation with sheet size.

- 5) The impedance on larger sheets appears to be more sensitive to movement along the dipole axis than to movement in the perpendicular direction.

9. REFERENCES

- 1 BURKE, G. J., 'Numerical Electromagnetics Code -NEC-4', UCRL-MA-109338, Jan. 1992
- 2 BELROSE, J. S., 'VLF, LF & MF Antennas', IEE Handbook of Antenna Design, Vol. 2, 1983, p 561-563
- 3 SCHELKUNOFF, S. A. and FRIIS, H. T., 'Antennas, Theory and Practice', John Wiley & Sons Inc., New York, 1952
- 4 McPHERSON, W. L., 'Reference Data for Radio Engineers', STC, London, 1948
- 5 SMITH, R. A., 'Aerials for Metre and Decimetre Wavelengths', Cambridge University Press, 1949, p 10

The Design of Planar Slot Arrays Revisited

J.C. Coetzee[†] and J. Joubert^{††}

[†] Department of Electrical Engineering, National University of Singapore, 4 Engineering Drive 3, Singapore 117576

^{††} Department Electrical & Electronic Engineering, University of Pretoria, Pretoria 0002, South Africa

Abstract

Design procedures for planar waveguide slot arrays have been known and used for years, but the inexperienced designer is often faced with a number of practical problems when trying to implement them, especially in the case of larger arrays consisting of sub-arrays. Some helpful hints concerning the numerical implementation are provided. These include an effective procedure to avoid the necessity of good initial guesses for the unknown dimensions and recommendations for the subdivision of the nonlinear equations into smaller groups. Other practical aspects which are not explicitly defined elsewhere in the literature, are also addressed.

1. INTRODUCTION

Planar slot arrays are key components of high performance airborne radar systems, and also find application in modern microwave communication systems. A planar array consists of a number of slotted waveguides arranged side-by-side, while the most popular way of feeding the individual branches is through the use of crossed waveguide couplers with centred-inclined slots. For large arrays, the concept of sub-arraying is often used to improve the usable frequency bandwidth, and also to reduce the sensitivity of antenna performance on dimensional tolerances. Each sub-array is then fed by a main line, while the individual main lines are fed by a beam forming network. Slotted array seeker antennas also make use of sub-arraying, where a monopulse comparator network effectively feeds the four quadrants of the antenna either in-phase or out of phase with respect to each other.

Design procedures for the synthesis of linear slot arrays were proposed by Elliott [1-3], and were later extended to cover planar arrays [4]. Other contributions to the field of array design include those of [5] and [6]. Even though these techniques have been known and used for years, the inexperienced designer is still faced with a number of practical problems when trying to implement them, especially in the case of larger arrays consisting of sub-arrays. In this paper, some helpful hints concerning the numerical implementation are provided, and other practical aspects which are not explicitly defined elsewhere in the literature are addressed.

The design procedure involves the repeated solution of sets of nonlinear equations in order to iteratively compute the offsets and lengths of the radiating slots, as well as the inclination angles and lengths of coupling slots. The successful numerical solution of sets of nonlinear equations is usually dependent on the quality of the initial guesses for the unknowns, the number

of unknowns and also on the nature of the nonlinear equations. In practice, specifying suitable starting values may require considerable effort. In this paper, a simple but highly effective method, which is less dependent on good initial guesses and a priori knowledge about the eventual geometry, is proposed.

It is known that the solution obtained for a specific design is not unique, due to a number of degrees of freedom. This aspect is usually addressed by fixing some of the dimensions. A different way of accommodating the redundancy is proposed. It naturally divides the nonlinear equations into smaller groups by effectively decoupling them into semi-independent sets which are solved individually during each iteration.

There also seems to be some uncertainty regarding the correct orientation of coupling slots, especially when the array has more than one feed line. Unequivocal relations for the signs of radiating slot offsets and coupling slot angles are thus provided. Finally, some guidelines on the specifications for beam-forming networks required by multi-sub-array systems are given.

2. THEORETICAL BACKGROUND

Consider a planar array consisting of a total of S sub-arrays. The s th sub-array shown in Fig. 1 consists of a total of T_s branch lines, while the t th branch line has a total of $N_{s,t}$ slots. The slots are resonantly spaced, i.e. $d = \lambda_g/2$ and $d_0 = \lambda_g/4$ at the design frequency, f_0 . The inter-slot spacing should be larger than the waveguide width, a , and for a waveguide filled with a dielectric material of relative permittivity ϵ_r , the value of a should be between the limits $\lambda_0/2\sqrt{\epsilon_r} \leq a \leq \lambda_0/\sqrt{2\epsilon_r}$, where λ_0 is the free space wavelength. The thickness of the septum separating neighboring branches is thus $t_0 = \lambda_g/2 - a$. The waveguide height, b , may be chosen arbitrarily. The sub-array is fed by means of a main line, which is connected to the different branch lines via centred-inclined coupling slots. The coupling slot feeding the t th branch line of the s th sub-array has an inclination angle of $\theta_{s,t}$ and a slot length of $l_{s,t}$. The angle $\theta_{s,t}$ is taken as positive in a clockwise direction. This coupling slot is located between the $k_{s,t}$ th and the $(k_{s,t}+1)$ th slot of the t th branch line. The term $\hat{u}_s = u_s \hat{x}$ is the unit vector in the direction toward the shorted end of the main line, so that $u_s = \pm 1$ for sub-arrays fed from the bottom and the top, respectively. The complete array has a total number of

$$M = \sum_{s=1}^S \sum_{t=1}^{T_s} N_{s,t} \text{ slots.}$$

Two distinct radiating slot indexing conventions are used:

- (a) A local numbering system with a triple index (s, t, n) denoting the n th slot in the t th branch line of the s th sub-array. The slot has a width of w , an offset of $x_{s,t,n}^{\text{off}}$ relative to the center line of the branch line, and a slot length of $L_{s,t,n}$. Slots in a branch line are numbered from left to right, irrespective of whether the sub-array is fed from the bottom (as in Fig. 1) or from the top. Branch lines are numbered such that the line closest to the feeding end is denoted by $t = 1$ and the line closest to the shorted end of the main line by $t = T_s$.

- (b) A global numbering system with a single index, i . The slot with local index (s, t, n) has a global index of

$$i = \sum_{u=1}^{s-1} \sum_{t=1}^{T_u} N_{u,t} + \sum_{v=1}^{t-1} N_{s,v} + n.$$

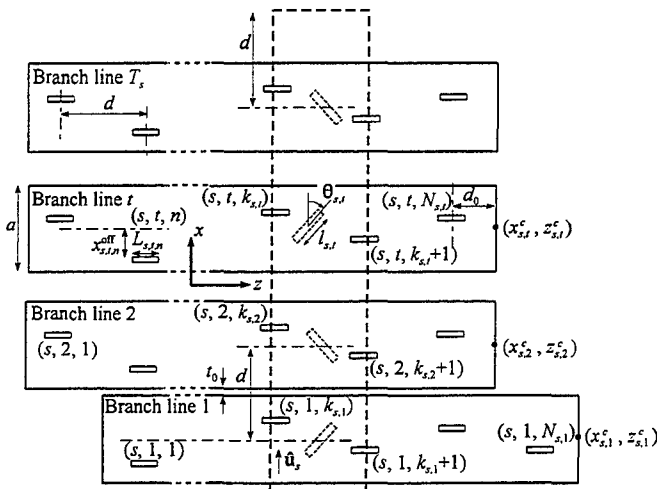


Fig. 1 Geometry of the s th sub-array.

The equivalent network for the n th branch line of the s th sub-array is shown in Fig. 2, where $y_{s,t,n}^a$ is the normalized active admittance of the n th slot. The design procedure involves the repeated solution of a set of nonlinear equations in order to determine the slot offsets and lengths. The nonlinear equations are related to the so-called design equations, given by [2]

$$y_{s,t,n}^a = K_1 f_{s,t,n} \frac{V_{s,t,n}^{\text{slot}}}{V_{s,t,n}} \quad (1)$$

and [3]

$$\frac{1}{y_{s,t,n}^a} = \frac{1}{y_{s,t,n}^{\text{self}}} + \frac{1}{(f_{s,t,n})^2 K_2} \sum_{j=1, j \neq i}^M \frac{V_j^{\text{slot}}}{V_i^{\text{slot}}} g_{ji} + \frac{1}{(f_{s,t,n})^2 K_3} \left[\frac{V_{s,t,n-1}^{\text{slot}}}{V_{s,t,n}^{\text{slot}}} h_{s,t,n} h_{s,t,n-1} + \frac{V_{s,t,n+1}^{\text{slot}}}{V_{s,t,n}^{\text{slot}}} h_{s,t,n} h_{s,t,n+1} \right] \quad (2)$$

For the slot with local index (s, t, n) and global index i , the slot voltage is denoted as $V_{s,t,n}^{\text{slot}}$ or V_i^{slot} , while the corresponding

voltage in the equivalent network is $V_{s,t,n}$. The term $y_{s,t,n}^{\text{self}} = y^{\text{self}}(x_{s,t,n}^{\text{off}}, L_{s,t,n})$ represents the normalized self-impedance of this slot. The function g_{ji} is given by [2], which is dependent on the coordinates of the centers of the i th and the j th slots. Let (x_i, z_i) the coordinates for the i th slot in the global coordinate system. In terms of the local coordinates, it is given by

$$(x_i, z_i) = (x_{s,t}^c + x_{s,t,n}^{\text{off}}, z_{s,t}^c - d_0 - N_{s,t}d + nd) \quad (3)$$

where $(x_{s,t}^c, z_{s,t}^c)$ are the coordinates of the center point of the right edge of the t th branch line. The functions $f_{s,t,n}$ and $h_{s,t,n}$ may be obtained from [2] and [3] by making the substitutions $2l_n = L_{s,t,n}$ and $x_n = x_{s,t,n}^{\text{off}}$. For $n = 1$ or $n = N_{s,t}$, the undefined terms in (2) such as $V_{s,t,0}^{\text{slot}}$, $V_{s,t,N_{s,t}+1}^{\text{slot}}$, $h_{s,t,0}$ and $h_{s,t,N_{s,t}+1}$ may be found through the application of image theory. The constants K_1 , K_2 and K_3 may also be obtained from [2] and [3].

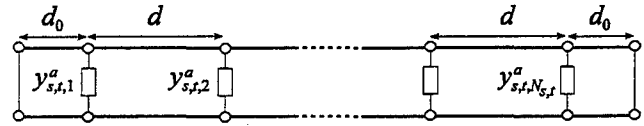


Fig. 2 Equivalent transmission line network for the n th branch line of the s th sub-array.

Let the voltages across the shunt elements in Fig. 2 be given by

$$V_{s,t,n} = q_{s,t} V_{s,t}^0 (-1)^{k_{s,t}-n} \quad (4)$$

The term $q_{s,t}$ is an arbitrary constant equal to ± 1 , depending on whether the offset of the slot with index $(s, t, k_{s,t})$ is to be positive or negative. These voltages are arbitrarily chosen to be real valued. Then $V_{s,t}^0$ is a positive real number representing the magnitude of the voltages on the equivalent circuit of the n th branch line of sub-array s .

The series impedances of the equivalent circuit for the main line in Fig. 3 are given by [4]

$$z^{(s,t)} = (\kappa^{(s,t)})^2 y_{\text{in}}^{(s,t)} \quad (5)$$

where $y_{\text{in}}^{(s,t)}$ is the normalized input admittance of the n th branch line of the s th sub-array, given by

$$y_{\text{in}}^{(s,t)} = \sum_{n=1}^{N_{s,t}} y_{s,t,n}^a \quad (6)$$

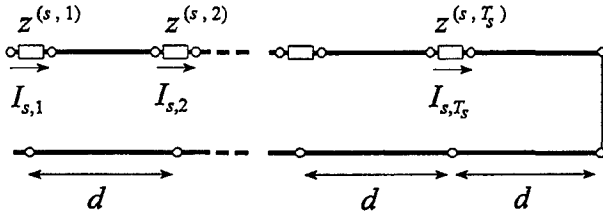


Fig. 3 Equivalent network for the main line of the s th sub-array.

The term $\kappa^{(s,t)}$ is the coupling coefficient defined by

$$\kappa^{(s,t)} = \sqrt{\frac{S_{11}^{(s,t)}}{1 - S_{11}^{(s,t)}}} \quad (7)$$

while $S_{11}^{(s,t)} = S_{11}(\theta = |\theta_{s,t}|, l = l_{s,t})$ is the scattering matrix component of the crossed waveguide couplers formed at the junction of the s th mainline and the t th branch line, as shown in Fig. 4. The normalized input impedance of the s th mainline is then given by

$$z_{in}^{(s)} = \sum_{t=1}^{T_s} z^{(s,t)} = \sum_{t=1}^{T_s} (\kappa^{(s,t)})^2 y_{in}^{(s,t)} \quad (8)$$

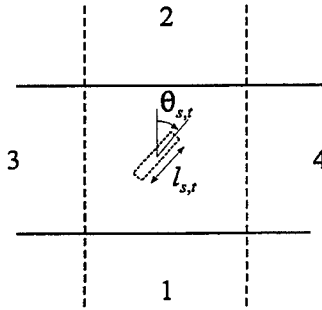


Fig. 4 Crossed-guide coupler geometry for the main line of the s th subarray and the t th stick.

Due to the fact that the coupling slots are also resonantly spaced (i.e. $d = \lambda_g/2$ at the design frequency, f_0), the current $I_{s,t}$ in Fig. 3 is given by

$$\begin{aligned} I_{s,t} &= (-1)^{t-1} I_{s,1} \\ &= (-1)^{t-1} \frac{2a^{(s)}}{\sqrt{Z_0}(z_{in}^{(s)} + 1)} \end{aligned} \quad (9)$$

where $I_{s,1}$ is the current at the first series element, while $a^{(s)}$ is the incident wave intensity. Suppose the input impedance of each sub-array is purely resistive. Then $z_{in}^{(s)} = r_{in}^{(s)}$, where $r_{in}^{(s)}$ is the chosen normalized input resistance of the s th sub-array as seen from the first series impedance in the main line equivalent circuit. The relation between the current at the

series impedance representing the t th coupling slot in the main line, $I_{s,t}$, and the voltage across the $k_{s,t}$ th element in the equivalent network for the t th branch line, $V_{s,t,k_{s,t}}$, is given by

$$V_{s,t,k_{s,t}} = u_s \frac{\theta_{s,t}}{|\theta_{s,t}|} \kappa^{(s,t)} I_{s,t} \quad (10)$$

One design objective is to have all the slot voltages in phase. From equation (1), it follows that the argument of the term $V_{s,t,k_{s,t}}/f_{s,t,n}$ should be uniform. In agreement with the choice of real-valued equivalent network voltages, this phase reference is taken to be zero. In a specific branch line, this is accomplished by alternating the offsets of the slots on opposite sides of the center line. The sign of the term $f_{s,t,k_{s,t}}$ will be equal to the value of $q_{s,t}$, which implies that the sign of $V_{s,t,k_{s,t}}$ should also be identical to the value of $q_{s,t}$. This agrees with the choice in (4). For resonant coupling slots, $\kappa^{(s,t)}$ is purely real, while (9) and (10) dictate that $a^{(s)}$ should also be real valued. Consequently, the orientations of the coupling slots are given by

$$\frac{\theta_{s,t}}{|\theta_{s,t}|} = (-1)^{t-1} u_s q_{s,t} \frac{a^{(s)}}{|a^{(s)}|} \quad (11)$$

Substituting (9) and (11) into (10) gives

$$V_{s,t,k_{s,t}} = q_{s,t} \kappa^{(s,t)} \frac{2|a^{(s)}|}{\sqrt{Z_0}(r_{in}^{(s)} + 1)} \quad (12)$$

A comparison of equations (4), (9) and (12) then yields the simple relation of [4], given by

$$V_{s,t}^0 = \kappa^{(s,t)} I_s^0 \quad (13)$$

where $I_s^0 = |I_{s,t}|$.

3. DERIVATION OF THE SETS OF NONLINEAR EQUATIONS

Consider the s th sub-array. Select the $k_{s,t}$ th slot branch line t to serve as the reference slot. From equations (1) and (4), it is found that

$$\frac{y_{s,t,n}^a}{y_{s,t,k_{s,t}}^a} = \frac{f_{s,t,n} V_{s,t,n}^{\text{slot}} (-1)^{n-k_{s,t}}}{f_{s,t,k_{s,t}} V_{s,t,k_{s,t}}^{\text{slot}}} \quad (14)$$

Note that the ratio in (14) is only dependant on the slot offsets and lengths in branch line t of sub-array s . Equation (14) does not provide a sufficient number of equations to uniquely solve for the unknown slot offsets and lengths in the branch. It has been suggested that the slot which is to have the greatest slot offset be singled out and assigned an offset near the upper limit of reliable input data [4]. However, it is often difficult to identify this slot without some degree of a priori knowledge of the eventual geometry, especially in cases of uniform

excitation. A different approach is to specify the input admittance of each branch line to be purely real and with a normalized input admittance of $g_{in}^{(s,t)}$. Equations (6) and (14) may then be used to construct the following set of $2N_{s,t}$ nonlinear equations for the unknown slot offsets and lengths of branch line t in sub-array s :

$$\operatorname{Re} \left[\frac{y_{s,t,n}^a - \frac{f_{s,t,n} V_{s,t,n}^{\text{slot}} (-1)^{n-k_{s,t}}}{f_{s,t,k_{s,t}} V_{s,t,k_{s,t}}^{\text{slot}}}}{y_{s,t,k_{s,t}}^a} \right] = 0$$

$$\operatorname{Im} [y_{s,t,n}^a] = 0 \quad n = 1, 2, \dots, N_{s,t} \quad n \neq k_{s,t} \quad (15)$$

$$g_{in}^{(s,t)} - \operatorname{Re} \left[\sum_{n=1}^{N_{s,t}} y_{s,t,n}^a \right] = 0$$

where $y_{s,t,n}^a$ is calculated using equation (2).

Comparing the active admittances of the $k_{s,t}$ th slot of the t th branch line and the $k_{s,1}$ th slot of the first branch line, using equations (1) and (12), results in

$$\frac{y_{s,t,k_{s,t}}^a}{y_{s,1,k_{s,1}}^a} = \frac{|f_{s,t,k_{s,t}}| V_{s,t,k_{s,t}}^{\text{slot}} \kappa^{(s,1)}}{|f_{s,1,k_{s,1}}| V_{s,1,k_{s,1}}^{\text{slot}} \kappa^{(s,t)}} \quad (16)$$

If the slot offsets and lengths of the reference slots are known, equations (8) and (16) may be used to construct the following set of $2T_s$ nonlinear equations for the magnitude of the inclination angles and coupling slot lengths of main line s :

$$\operatorname{Re} \left[\frac{y_{s,t,k_{s,t}}^a - \frac{|f_{s,t,k_{s,t}}| V_{s,t,k_{s,t}}^{\text{slot}} \kappa^{(s,1)}}{|f_{s,1,k_{s,1}}| V_{s,1,k_{s,1}}^{\text{slot}} \kappa^{(s,t)}}}{y_{s,1,k_{s,1}}^a} \right] = 0 \quad t = 2, 3, \dots, T_s$$

$$\operatorname{Im} [\kappa^{(s,t)}] = 0 \quad t = 1, 2, \dots, T_s \quad (17)$$

$$\operatorname{Re} \left[r_{in}^{(s)} - \sum_{t=1}^{T_s} (\kappa^{(s,t)})^2 g_{in}^{(s,t)} \right] = 0$$

where $\kappa^{(s,t)}$ is calculated using (7).

4. EFFECTIVE IMPLEMENTATION OF THE STARTING VALUE PROBLEM

Depending on the nature of a set of nonlinear equations, their numerical solution may be highly dependent on the quality of the initial guesses for the unknowns, as well as the number of unknowns. In the previous section, the equations were subdivided into smaller sets, but the designer is still faced with finding good starting values of the unknown slot dimensions.

For larger arrays, the evaluation of the external mutual coupling terms g_{ji} is generally the most time consuming step in the numerical implementation of a design procedure. For

practical purposes, an iterative approach for the design of linear arrays was proposed in [2], where during each iteration, these terms are computed using the current set of slot dimensions and are assumed to remain constant while calculating new dimensions by way of solving of a set of nonlinear equations. It was also suggested in [4] that the external and internal mutual coupling terms be set to zero for the first iteration. Due to the simplified nature of the resulting nonlinear equations, this negates the need for good initial guesses for the unknown as required by nonlinear equation solvers. Arbitrary starting values within the realistic range of slot dimensions may then be specified, while the nonlinear equation solver routine is usually successful in finding a solution. During the second iteration, the computed slot dimensions for the zero mutual coupling case are used to re-evaluate the mutual coupling terms, and the same dimensions are employed as starting values for the subsequent solution of the nonlinear equations. This approach is entirely effective for linear arrays. This is due to the fact that the mutual coupling between slots that are approximately axially aligned is relatively small, and therefore the abrupt inclusion of the mutual coupling contributions during the second iteration only has a secondary effect, and the changes in slot dimensions never become excessive.

For planar arrays the displacement between certain slots is also lateral, which causes the external mutual coupling to have a more pronounced effect on the slot dimensions. The examples in [3] bare evidence of this. Even though a uniform excitation for all slots was specified, the mutual coupling causes large variations in slot offsets, while in the absence of mutual coupling, all slots have the same lengths and offset magnitudes. Implementation of the approach proposed for linear arrays may result in numerical instability. Problems generally do not occur when solving for the zero mutual coupling case during the first iteration. However, during the second iteration where the zero mutual coupling dimensions (which may differ appreciably from the final results) are used to first calculate g_{ji} and then also as starting values for the subsequent solving of the nonlinear equations, the procedure often fails.

It is therefore proposed that the procedure be modified by retaining the first iteration with zero mutual coupling, but instead of abruptly introducing the effects of mutual coupling during the second iteration, that its effects be included gradually. This is achieved by weighing the values of g_{ji} and $h_{s,t,n}$ with a weighting factor increasing from 0 to 1 during the first half of a chosen total number of iterations. Consequently, the first iteration will be performed with zero mutual coupling, while the full effect of the mutual coupling is only included during the second half of the iterations. This approach generously compensates for a possible increase in the total number of iterations by being very robust and reliable. The ease of implementation of this procedure is also an advantage

over other approaches which merely rely on good starting values that are obtained by for instance first considering an infinite array [6].

5. BEAM-FORMING NETWORK

An array consisting of a number of sub-arrays would naturally require a power splitter or beam-forming network to distribute the power from the antenna input to the multiple sub-array main lines. A complete design should therefore also include the specifications of the power splitter network. A comparison of the active admittances of the $k_{s,1}$ th slot of the first branch line of sub-array s and of the $k_{1,1}$ th slot of the first branch line of sub-array 1 using equations (1) and (12) yields the following relative amplitudes of the incident wave intensities for the sub-arrays:

$$\frac{|a^{(s)}|}{|a^{(1)}|} = \frac{|f_{s,1,k_{s,1}}| V_{s,1,k_{s,1}}^{\text{slot}} \kappa^{(1,1)} y_{1,1,k_{1,1}}^a (r_{\text{in}}^{(s)} + 1)}{|f_{1,1,k_{1,1}}| V_{1,1,k_{1,1}}^{\text{slot}} \kappa^{(s,1)} y_{s,1,k_{s,1}}^a (r_{\text{in}}^{(1)} + 1)} \quad (18)$$

The phase difference between $a^{(s)}$ and $a^{(1)}$ is either 0° or 180° . The phase relation is chosen in accordance with the phase properties of the beam-forming network to be used. Together with (18), the ratio $a^{(s)}/a^{(1)}$ is thus completely specified. In general, an array consisting of S sub-arrays would require a splitter with $P = S + 1$ ports. For the sake of clarity, it is assumed that each of the first S ports is connected to its corresponding sub-array, while the P th port serves as the common feed port. From the definition of the scattering parameters, it follows that

$$[S^{\text{split}}] [a^{\text{split}}] = [b^{\text{split}}] \quad (19)$$

$[S^{\text{split}}]$ is the $P \times P$ scattering parameter matrix of the network, specified with the phase reference of port 1 to port S at the center of the first coupling slot of the main line it is connected to. Since the first S ports of the splitter network are terminated in the input impedances of the sub-arrays, it follows that

$$a_s^{\text{split}} = \Gamma_{\text{in}}^{(s)} b_s^{\text{split}} \quad s = 1, 2, \dots, S \quad (20)$$

where

$$\Gamma_{\text{in}}^{(s)} = \frac{r_{\text{in}}^{(s)} - 1}{r_{\text{in}}^{(s)} + 1} \quad (21)$$

The wave emanating from the s th port is fed directly into the main line of the s th sub-array, while the antenna should normally be matched at port P . This implies that

$$b_s^{\text{split}} = \begin{cases} a^{(s)} & s = 1, 2, \dots, S \\ 0 & s = P \end{cases} \quad (22)$$

For a lossless splitter network, the conservation of power condition requires that

$$\sum_{s=1}^P (|a_s^{\text{split}}|^2 - |b_s^{\text{split}}|^2) = 0 \quad (23)$$

Using (22) and (23) together with the specification for $a^{(s)}/a^{(1)}$ then gives

$$\frac{b_s^{\text{split}}}{a_p^{\text{split}}} = \begin{cases} \frac{\frac{a^{(s)}}{a^{(1)}} e^{j\zeta}}{\sqrt{\sum_{m=1}^S \left(\frac{a^{(m)}}{a^{(1)}}\right)^2 [1 - \Gamma_{\text{in}}^{(m)2}]}} & s = 1, 2, \dots, S \\ 0 & s = P \end{cases} \quad (24)$$

ζ is an arbitrary common phase term. The relations in (24) specify the requirements for the splitter network. The simplest way of realizing this would be to design the sub-arrays to be matched (i.e. $r_{\text{in}}^{(s)} = 1$ and $\Gamma_{\text{in}}^{(s)} = 0$), which would then require that

$$S_{sP}^{\text{split}} = \begin{cases} \frac{(a^{(s)}/a^{(1)}) e^{j\zeta}}{\sqrt{\sum_{m=1}^S (a^{(m)}/a^{(1)})^2}} & s = 1, 2, \dots, S \\ 0 & s = P \end{cases} \quad (25)$$

6. DESIGN PROCEDURE

Array design requires data on the self admittance of isolated radiating slots as a function of the slot offset and length, as well as scattering parameters for coupling slots in terms of the inclination angle and slot length. These may either be obtained through measurement or calculation. In the case of the latter, the formulations in [7] and [8] may be used to precompute the databases, while a bivariate spline interpolation scheme as in [9] has proved to be very effective for the calculation of the terms $y_{s,t,n}^{\text{self}} = y^{\text{self}}(x_{s,t,n}^{\text{off}}, L_{s,t,n})$ and $\kappa^{(s,t)} = \kappa(|\theta_{s,t}|, l_{s,t})$. The design procedure then consists of the following:

1. Specify the slot voltages $V_{s,t,n}^{\text{slot}}$ for a desired radiation pattern.
2. Specify u_s for each sub-array, as well as $q_{s,t}$ and $k_{s,t}$ for each branch line.
3. Select realistic values for the input conductance of each branch line, $g_{\text{in}}^{(s,t)}$. A guideline is to choose a typical slot offset $x_{\text{typ}}^{\text{off}}$ and to identify the corresponding resonant length for this offset, L_{typ} . A typical value for the input conductance would then be $g_{\text{in}}^{(s,t)} = N_{s,t} \cdot y^{\text{self}}(x_{\text{typ}}^{\text{off}}, L_{\text{typ}})$.
4. Specify the input resistance of each main line, $r_{\text{in}}^{(s)}$. Unless the circumstances dictate otherwise, the most convenient choice would be $r_{\text{in}}^{(s)} = 1$.
5. Select an appropriate number of iterations to be performed, C , where $C \geq 10$ is an even-valued integer.
6. Select initial guesses for the lengths and offsets for the

radiating slots. An effective choice is to select $x_{s,t,n}^{\text{off}} = (-1)^{k_{s,t,n}} q_{s,t} x_{\text{typ}}^{\text{off}}$ and $L_{s,t,n} = L_{\text{typ}}$.

7. Select initial guesses for the magnitude of the inclination angles and slot lengths for the coupling slots.
8. Set the iteration counter $c = 1$.
9. Calculate the global slot coordinates using equation (3).
10. Calculate the mutual coupling terms g_{ji} and $h_{s,t,n}$.
11. For the first half of the total number of iterations ($c \leq C/2$), weigh the values of g_{ji} and $h_{s,t,n}$ with a factor of $2(c-1)/C$, i.e. scale all the elements of g_{ji} to $2(c-1)g_{ji}/C$ and the elements of $h_{s,t,n}$ to $2(c-1)h_{s,t,n}/C$.
12. Set $s = 1$.
13. Set $t = 1$.
14. Solve the set of $2N_{s,t}$ nonlinear equations in (15) for the unknown slot offsets and lengths of branch line t in sub-array s : $(x_{s,t,n}^{\text{off}}, L_{s,t,n})$ where $n = 1, 2, \dots, N_{s,t}$.
15. Increment t and repeat step 14 until $t = T_s$.
16. Solve the set of $2T_s$ nonlinear equations in (17) for the magnitude of the inclination angles and coupling slot lengths in main line s : $(|\theta_{s,t}|, l_{s,t})$ where $t = 1, 2, \dots, T_s$.
17. Increment s and repeat steps 13-16 until $s = S$.
18. Increment c and repeat steps 9-17 until $c = C$.
19. Calculate the ratios of the wave intensities that a power splitter network needs to supply to the different sub-arrays from (18).
20. Specify the phase relation at each of the first S ports of the power splitter, i.e. whether sub-arrays are to be fed in phase or 180° out of phase relative to the excitation of the first sub-array, and use (11) to determine the orientation of the coupling slots.

7. DESIGN EXAMPLE

As an example, a small array similar to the one shown in Fig. 5 was designed. It consists of four sub-arrays, each having three branches and three slots per branch. A design frequency of $f_0 = 9$ GHz was chosen, and half-height X-band waveguide of width $a = 22.86$ mm and height $b = 5.08$ mm was used for the branch guides and feed lines. A database for the properties of isolated radiating slots and inclined coupling slots was computed, using a slot width of $w = 1.5875$ mm and a waveguide wall thickness of $t = 1.27$ mm. A uniform excitation for all radiators was adopted. The array was designed to have a normalized conductance of $g_{\text{in}}^{(s,t)} = 1.5$ for all branches, and a normalized input resistance of $r_{\text{in}}^{(s)} = 1$ for each of the four sub-arrays. From the geometry, it follows that $u_1 = u_2 = -1$, $u_3 = u_4 = 1$, $k_{1,t} = k_{4,t} = 1$, $k_{2,t} = k_{3,t} = 2$ and $q_{s,t} = -1$. A total number of ten iterative steps were used during the design. The computed slot offsets and slot lengths for the radiating slots are shown in Table I, while the inclination angles and lengths of the coupling slots are listed in Table II. Due to the symmetry, sub-arrays 1 and 3 and sub-arrays 2 and 4 are mirror images of each other, and therefore corresponding slots will have the same magnitude of offset or

inclination angle, but with a difference in sign.

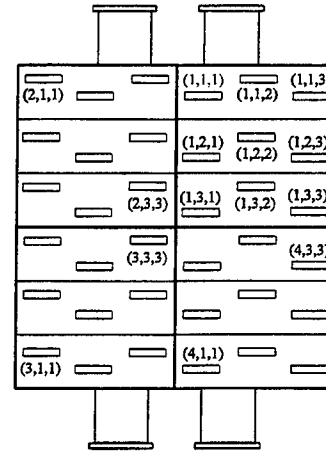


Fig. 5 Geometry of a 4×3 array.

Table I Slot offsets and slot lengths of radiating slots.

Slot index (s, t, n)	$x_{s,t,n}^{\text{off}}$ (mm)	$L_{s,t,n}$ (mm)
(1,1,1), (3,1,3)	∓ 2.256	16.758
(1,1,2), (3,1,2)	± 3.015	16.821
(1,1,3), (3,1,1)	∓ 2.397	16.779
(1,2,1), (3,2,3)	∓ 2.859	16.822
(1,2,2), (3,2,2)	± 1.958	16.287
(1,2,3), (3,2,1)	∓ 2.221	16.574
(1,3,1), (3,3,3)	∓ 2.177	16.842
(1,3,2), (3,3,2)	± 1.516	16.787
(1,3,3), (3,3,1)	∓ 2.325	16.830
(2,1,1), (4,1,3)	± 2.848	16.828
(2,1,2), (4,1,2)	∓ 2.012	16.630
(2,1,3), (4,1,1)	± 3.138	16.923
(2,2,1), (4,2,3)	± 1.976	16.437
(2,2,2), (4,2,2)	∓ 2.679	16.610
(2,2,3), (4,2,1)	± 2.153	16.500
(2,3,1), (4,3,3)	± 1.969	16.888
(2,3,2), (4,3,2)	∓ 2.188	16.756
(2,3,3), (4,3,1)	± 1.603	16.885

Table II Inclination angles and slot lengths of coupling slots.

Slot index (s, t)	$\theta_{s,t}$ (degrees)	$l_{s,t}$ (mm)
(1,1), (3,1)	± 23.61	16.986
(1,2), (3,2)	∓ 21.47	16.970
(1,3), (3,3)	± 18.58	16.948
(2,1), (4,1)	± 24.73	16.998
(2,2), (4,2)	∓ 20.81	16.964
(2,3), (4,3)	± 17.88	16.943

Due to the symmetry, the incident wave intensities were found to be $a^{(s)}/a^{(1)} = 1$ for all sub-arrays.

The effect of the gradual inclusion of the mutual coupling is illustrated in Fig. 6, where the variation of the offset for the slot with index (1,3,2) as computed during the iterative steps is shown. The initial offset calculated for the case with zero mutual coupling is 3.082 mm, while the final offset is only 1.516 mm. The gradual introduction of the mutual coupling contributions over the next five iterative steps avoids abrupt changes in the slot dimensions, and convergence is easily achieved during the second half of the iterations.

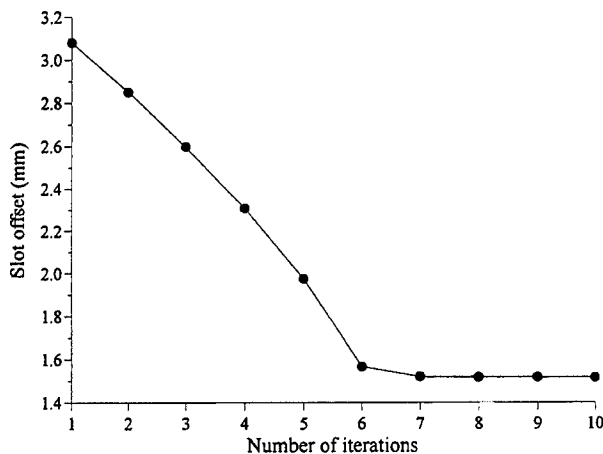


Fig. 6 Offset of slot (1,3,2) as computed during each iterative step.

8. CONCLUSION

The repeated computation of the external mutual coupling between slots, which involves numerical integration, is the most time-consuming part of the procedure. Utilization of an alternative expression for the coupling coefficient [10] results in an appreciable increase in efficiency. Some numerical experimentation may be required in order to obtain a design where all the slot offsets are within the desirable range. Slot offsets of less than $w/2$ should be avoided. Care should also be taken not to allow the offsets to become too large, especially when using waveguides of reduced height. This may lead to problems related to the validity of the equivalent circuit models for the slots [11]. If the computed offsets of a particular branch are either too large or too small, the input conductance of those branches should be decreased or increased and the design repeated. Used in conjunction with an analysis procedure [12], the admittance levels of the branch lines may be chosen so as to optimize the off-centre frequency performance of the array.

The proposed algorithm is easily translated into computer code, and has been applied successfully to the design of arrays of varying sizes. The process of subdividing the nonlinear equations into smaller groups and gradually introducing the

effects of mutual coupling has proven to be very reliable when used in conjunction with reliable nonlinear equation solver routines.

REFERENCES

- [1] R.S. Elliott and L.A. Kurtz, "The Design of Small Slot Arrays", *IEEE Trans. Antennas Propagat.*, vol. AP-26, no. 3, pp. 214-219, Mar. 1978
- [2] R.S. Elliott, "An Improved Design Procedure for Small Arrays of Shunt Slots", *IEEE Trans. Antennas Propagat.*, vol. AP-31, no. 1, pp. 48-53, Jan. 1983.
- [3] R.S. Elliott, "The Design of Slot Arrays Including Internal Mutual Coupling", *IEEE Trans. Antennas Propagat.*, vol. AP-34, no. 9, pp. 1149-1154, Sept. 1986.
- [4] R.S. Elliott, "The Design of Waveguide-Fed Slot Arrays", in Y.T. Lo and S.W. Lee (Edits.), *Antenna Handbook*, Van Nostrand Reinhold, 1988.
- [5] A.J. Angster and A.H.I. McCormick, "Theoretical design and synthesis of slotted waveguide arrays", *IEE Proc. H Microwaves, Antenna & Propag.*, vol. 136, no. 1, pp. 39-46, Feb. 1989.
- [6] H. Y. Yee, "The Design of Large Waveguide Arrays of Shunt Slots", *IEEE Trans. Antennas Propagat.*, vol. 40, no. 7, pp. 775-781, July 1992.
- [7] L.G. Josefson, "Analysis of Longitudinal Slots in Rectangular Waveguides", *IEEE Trans. Antennas Propagat.*, Vol. AP-35, pp. 1351-1357, Dec. 1987.
- [8] W. Hanyang and W. Wei, "Moment method analysis of a feeding system in a slotted-waveguide antenna", *IEE Proc. H Microwaves, Antenna & Propag.*, Vol. 135, pp. 313-318, Oct. 1988.
- [9] D.A. McNamara and J. Joubert, "On The Use of Bivariate Spline Interpolation of Slot Data in the Design of Slotted Waveguide Arrays", *ACES J.*, vol. 9, no. 1, pp. 6-9, 1994.
- [10] G. Mazzarella and G. Panariello, "Fast computation of mutual coupling in slot arrays", *Microwave J.*, pp. 193-196, June 1988.
- [11] G.J. Stern and R.S. Elliott, "Resonant Length of Longitudinal Slots and Validity of Circuit Representation: Theory and Experiment", *IEEE Trans. Antennas Propagat.*, vol. AP-33, no. 11, pp. 1264-1271, Nov. 1985
- [12] J.C. Coetzee, J. Joubert and D.A. McNamara, "Off-Center-Frequency Analysis of a Complete Planar Slotted Waveguide Array Consisting of Sub-Arrays", submitted for publication in *IEEE Trans. Antennas Propagat.*

'2000 INSTITUTIONAL MEMBERS

ADVANSIS, INC.
20370 Town Center
Cupertino, CA 95014

ALGON MOBILE COMM.
Nasvagen 17
Akersberga, SWEDEN S-18425

ANDREW CORPORATION
10500 W. 153rd Street
Orland Park, IL 60462

AUSTRALIAN DEFENCE LIB.
Northcott Drive
Campbell, A.C.T. AUSTRALIA 2600

BOEING CO, RENTON TECH LIB
PO Bos 3707
Seattle, WA 98124-2207

BOEING NORTH AMERICAN SVCS
1745 Jefferson Davis Hwy
Arlington, VA 22202

BPLUS
100 University Court, PO B 1428
Blackwood, NJ 08012

BRITISH AEROSPACE
Newport Road
Isle of Wight, PO 318 PF UK

BRITISH AEROSPACE
FPC 267 PO Box 5
Filton, BRISTOL, BS12 7QW UK

CENTER HP COMPUTING
PO Box 830657
Birmingham, AL 35283-0657

CHALMERS UNIV of TECHNOLOGY
Dept of Microwave Technology
Gothenburg, SWEDEN S 41296

CHIHUAHUA UNIVERSITY
P.O. Box 830657
Birmingham, AL 35283-0657

CST GMBH
Lauteschlagerstrasse 38
Darmstadt, GERMANY D-64289

CULHAM SCIENCE LAB
UK Atomic Energy Authority
Abingdon, OXFORD, OX14 3DB UK

DARTMOUTH COLLEGE
Feldberg Library
6193 Murdough Ctr.
Hanover, NH 03755-3560

DEFENCE TECH & PROCUREMENT
NEMP LAB
SPIEZ, SWITZERLAND CH 3700

DEFENSE RESEARCH ESTAB. LIB.
3701 Carling Avenue
Ottawa, ON, K1A 0Z4 CANADA

DEUTSCHE TELEKOM AG
PO Box 10-00-03
Darmstadt, D-64 276 GERMANY

E.T.S.E. TELECOMUNICACIONES
Campus Lagoas Marcosende
Vigo, 36200 SPAIN

ELECTRICAL COMM LIBRARY
1-1 Hikarinooka
Kanagawa, Ken, 239-0847 JAPAN

ERICSSON SAAB
Gelbgjutaregat
Linkoping, SWEDEN SE 58188

FACOLTA INGEGNERIA
Library, Via G Duranti 89
Perugia, ITALY 06125

FANFIELD LTD
Braxted Park
Witham, Essex, CM8 3XB UK

FIRSTMARK TECHNOLOGIES
85 St. Charles Quest St.
Longueuil, PQ, J4H 1C5 CANADA

FUNDAÇÃO CPqD, BIBLIOTECA
Rod. Campinas M
Campinas, SP, BRAZIL 13083-970

GEC MARCONI RES. CTR. LIB.
W. Hanningfield Road, Gt. Baddow
Chelmsford, ESSEX, CM2 8HN UK

GEORGIA TECH LIBRARY
225 North Avenue, NW
Atlanta, GA 30332-0001

HARRIS CORP
1680 University Avenue
Rochester, NY 14610-9983

HKUST, UNIVERSITY LIBRARY
Clear Water Bay Road
Kowloon, HONG KONG

HRL LIBRARY
3011 Malibu Canyon Road
Malibu, CA 90265-4737

HUNTING ENGINEERING LTD.
Reddings Wood, Ampthill
Bedford, MK45 2HD UK

IIT RESEARCH INSTITUTE
185 Admiral Cochrane Drive
Annapolis, MD 21401-7396

IMAGINEERING LTD.
1090 Don Mills Road
Toronto, M3C 3R6, CANADA

IPS RADIO & SPACE SVC/LIBRARY
PO Box 5606
W. Chatswood, 2057 AUSTRALIA

KARGER PUBLISHING
PO Box 888
Unionville, CT 06085-0888

KATHREIN-WERKE
PO Box 100 444
Rosenheim, D-83004 GERMANY

LINDA HALL LIBRARY
5109 Cherry Street
Kansas City, MO 64110-2498

MISSISSIPPI STATE UNIV LIBRARY
PO Box 9570
Mississippi State, MS 39762

MIT LINCOLN LAB LIBRARY
244 Wood Street
Lexington, MA 02173-0073

MITRE CORPORATION LIBRARY
202 Burlington Road
Bedford, MA 01730-1407

MOD (PE)
Mod Abbey Wood
Stoke Gifford, BS34 8JH UK

MYERS ENGINEERING INTL.
PO Box 15908, 5425 NW 24th St.
Margate, FL 33063

NATIONAL AEROSPACE LAB, NLR
Anthony Fokkerweg 2
Emmeloord, 8300 NETHERLANDS

NATL RADIOLOGICAL PROT. BD.
Chilton
Didcot, OXON, OX11 0RG UK

NAVAL RESEARCH LABORATORY
C. Office
Washington, DC 20375

NEMP -LABOR SPIEZ LABS
Nemp Laboratory
Spiez, CH 3700 SWITZERLAND

NGIC
220 7th Street, NE
Charlottesville, VA 22902-5396

NNR AIR CARGO SERVICE
Hook Creed Blvd. & 145th Avenue
Valley Stream, NY 11581

NORTEL TECHNOLOGY
London Road
Harlow, ESSEX, CM17 9NA UK

PENN STATE UNIVERSITY LIB.
Pattee Library
University Park, PA 16802

PHILIPS RESEARCH LAB LIBRARY
Cross Oak Lane, Salfords
Redhill, SURREY, RH1 5HA UK

QUEEN MARY & WESTFIELD COLL
Mile End Road
London E1 4NS UK

QUEENSLAND CENTER, LIBRARY
2643 Moggill Road
Brisbane, Qld, 4069 AUSTRALIA

RAND AFRIKAANS UNIVERSITY
PO Box 524, Aucklandpark
Johannesburg, 2006 S AFRICA

READMORE ACADEMIC SVCS.
LIBRARY
901 Route 168
Turnersville, NY 08012

SALISBURY DSTO
PO Box 830701
Birmingham, AL 35283-0701

SESTRA STRADA, CRS4
BIBLIOTECA
Casella Postale
Uta, ITALY 09010

SONY CORPORATION
174 Fujitsukacho, Hodogaya Ku
Yokohama MZ, 240 JAPAN

SOUTHWEST RESEARCH INST.
6220 Culebra Road
San Antonio, TX 78238

SPIKE TECH
1 Chestnut Street
Nashua, NH 03060

SWETS SUBSCRIPTION SERVICE
440 Creamery Way, Suite A
Exton, PA 19341

TASC - LIBRARY
55 Walkers Brook Drive
Reading, MA 01867-3297

TECHNISCHE UNIV. DELFT
Mekelweg 4, Delft
HOLLAND, 2628 CD
NETHERLANDS

TELSTRA RES. LABS LIBRARY
770 Blackburn Road
Clayton, VIC, 3168 AUSTRALIA

UNIV OF CENTRAL FLORIDA LIB.
PO Box 162440
Orlando, FL 32816-2440

UNIV OF COLORADO LIBRARY
Campus Box 184
Boulder, CO 80309-0184

UNIV OF MISSOURI-ROLLA LIB.
1870 Miner Circle
Rolla, MO 65409-0001

UNIVERSITY OF SAO PAULO
Av Prof Luciano
Sao Paulo, 05508-

UNIVERSITY OF WARWICK
Gibbet Hill Road
Coventry, CV4 7AL UK

US ARMY COLD REGION RES, LIB.
72 Lyme Road
Hanover, NH 03775-1290

US COAST GUARD ACADEMY
15 Mohegan Avenue
New London, CT 06320-4195

VECTOR FIELDS LTD.
24 Bankside Kidlington
Oxford, OX5 1JE UK

VIT, TECHNICAL RESEARCH. CTR.
PO Box 1202
Espoo, FIN-02044 FINLAND

ACES COPYRIGHT FORM

This form is intended for original, previously unpublished manuscripts submitted to ACES periodicals and conference publications. The signed form, appropriately completed, MUST ACCOMPANY any paper in order to be published by ACES. PLEASE READ REVERSE SIDE OF THIS FORM FOR FURTHER DETAILS.

TITLE OF PAPER:

AUTHORS(S)

PUBLICATION TITLE/DATE:

RETURN FORM TO:

Dr. Richard W. Adler
Naval Postgraduate School
Code EC/AB
833 Dyer Road, Room 437
Monterey, CA 93943-5121 USA

PART A - COPYRIGHT TRANSFER FORM

(NOTE: Company or other forms may not be substituted for this form. U.S. Government employees whose work is not subject to copyright may so certify by signing Part B below. Authors whose work is subject to Crown Copyright may sign Part C overleaf).

The undersigned, desiring to publish the above paper in a publication of ACES, hereby transfer their copyrights in the above paper to The Applied Computational Electromagnetics Society (ACES). The undersigned hereby represents and warrants that the paper is original and that he/she is the author of the paper or otherwise has the power and authority to make and execute this assignment.

Returned Rights: In return for these rights, ACES hereby grants to the above authors, and the employers for whom the work was performed, royalty-free permission to:

1. Retain all proprietary rights other than copyright, such as patent rights.
2. Reuse all or portions of the above paper in other works.
3. Reproduce, or have reproduced, the above paper for the author's personal use or for internal company use provided that (a) the source and ACES copyright are indicated, (b) the copies are not used in a way that implies ACES endorsement of a product or service of an employer, and (c) the copies per se are not offered for sale.
4. Make limited distribution of all or portions of the above paper prior to publication.
5. In the case of work performed under U.S. Government contract, ACES grants the U.S. Government royalty-free permission to reproduce all or portions of the above paper, and to authorize others to do so, for U.S. Government purposes only.

ACES Obligations: In exercising its rights under copyright, ACES will make all reasonable efforts to act in the interests of the authors and employers as well as in its own interest. In particular, ACES REQUIRES that:

1. The consent of the first-named author be sought as a condition in granting re-publication permission to others.
2. The consent of the undersigned employer be obtained as a condition in granting permission to others to reuse all or portions of the paper for promotion or marketing purposes.

In the event the above paper is not accepted and published by ACES or is withdrawn by the author(s) before acceptance by ACES, this agreement becomes null and void.

AUTHORIZED SIGNATURE

TITLE (IF NOT AUTHOR)

EMPLOYER FOR WHOM WORK WAS PERFORMED

DATE FORM SIGNED

PART B - U.S. GOVERNMENT EMPLOYEE CERTIFICATION

(NOTE: If your work was performed under Government contract but you are not a Government employee, sign transfer form above and see item 5 under Returned Rights).

This certifies that all authors of the above paper are employees of the U.S. Government and performed this work as part of their employment and that the paper is therefore not subject to U.S. copyright protection.

AUTHORIZED SIGNATURE

TITLE (IF NOT AUTHOR)

NAME OF GOVERNMENT ORGANIZATION

DATE FORM SIGNED

PART C - CROWN COPYRIGHT

(Note: ACES recognizes and will honor Crown Copyright as it does U.S. Copyright. It is understood that, in asserting Crown Copyright, ACES in no way diminishes its rights as publisher. Sign only if ALL authors are subject to Crown Copyright.

This certifies that all authors of the above Paper are subject to Crown Copyright. (Appropriate documentation and instructions regarding form of Crown Copyright notice may be attached).

AUTHORIZED SIGNATURE

TITLE OF SIGNEE

NAME OF GOVERNMENT BRANCH

DATE FORM SIGNED

Information to Authors

ACES POLICY

ACES distributes its technical publications throughout the world, and it may be necessary to translate and abstract its publications, and articles contained therein, for inclusion in various compendiums and similar publications, etc. When an article is submitted for publication by ACES, acceptance of the article implies that ACES has the rights to do all of the things it normally does with such an article.

In connection with its publishing activities, it is the policy of ACES to own the copyrights in its technical publications, and to the contributions contained therein, in order to protect the interests of ACES, its authors and their employers, and at the same time to facilitate the appropriate re-use of this material by others.

The new United States copyright law requires that the transfer of copyrights in each contribution from the author to ACES be confirmed in writing. It is therefore necessary that you execute either Part A-Copyright Transfer Form or Part B-U.S. Government Employee Certification or Part C-Crown Copyright on this sheet and return it to the Managing Editor (or person who supplied this sheet) as promptly as possible.

CLEARANCE OF PAPERS

ACES must of necessity assume that materials presented at its meetings or submitted to its publications is properly available for general dissemination to the audiences these activities are organized to serve. It is the responsibility of the authors, not ACES, to determine whether disclosure of their material requires the prior consent of other parties and if so, to obtain it. Furthermore, ACES must assume that, if an author uses within his/her article previously published and/or copyrighted material that permission has been obtained for such use and that any required credit lines, copyright notices, etc. are duly noted.

AUTHOR/COMPANY RIGHTS

If you are employed and you prepared your paper as a part of your job, the rights to your paper initially rest with your employer. In that case, when you sign the copyright form, we assume you are authorized to do so by your employer and that your employer has consented to all of the terms and conditions of this form. If not, it should be signed by someone so authorized.

NOTE RE RETURNED RIGHTS: Just as ACES now requires a signed copyright transfer form in order to do "business as usual", it is the intent of this form to return rights to the author and employer so that they too may do "business as usual". If further clarification is required, please contact: The Managing Editor, R.W. Adler, Naval Postgraduate School, Code EC/AB, Monterey, CA, 93943, USA (408)656-2352.

Please note that, although authors are permitted to re-use all or portions of their ACES copyrighted material in other works, this does not include granting third party requests for reprinting, republishing, or other types of re-use.

JOINT AUTHORSHIP

For jointly authored papers, only one signature is required, but we assume all authors have been advised and have consented to the terms of this form.

U.S. GOVERNMENT EMPLOYEES

Authors who are U.S. Government employees are not required to sign the Copyright Transfer Form (Part A), but any co-authors outside the Government are.

Part B of the form is to be used instead of Part A only if all authors are U.S. Government employees and prepared the paper as part of their job.

NOTE RE GOVERNMENT CONTRACT WORK: Authors whose work was performed under a U.S. Government contract but who are not Government employees are required to sign Part A-Copyright Transfer Form. However, item 5 of the form returns reproduction rights to the U.S. Government when required, even though ACES copyright policy is in effect with respect to the reuse of material by the general public.

APPLIED COMPUTATIONAL ELECTROMAGNETICS SOCIETY JOURNAL

INFORMATION FOR AUTHORS

PUBLICATION CRITERIA

Each paper is required to manifest some relation to applied computational electromagnetics. **Papers may address general issues in applied computational electromagnetics, or they may focus on specific applications, techniques, codes, or computational issues.** While the following list is not exhaustive, each paper will generally relate to at least one of these areas:

- 1. Code validation.** This is done using internal checks or experimental, analytical or other computational data. Measured data of potential utility to code validation efforts will also be considered for publication.
- 2. Code performance analysis.** This usually involves identification of numerical accuracy or other limitations, solution convergence, numerical and physical modeling error, and parameter tradeoffs. However, it is also permissible to address issues such as ease-of-use, set-up time, run time, special outputs, or other special features.
- 3. Computational studies of basic physics.** This involves using a code, algorithm, or computational technique to simulate reality in such a way that better or new physical insight or understanding is achieved.
- 4. New computational techniques,** or new applications for existing computational techniques or codes.
- 5. "Tricks of the trade"** in selecting and applying codes and techniques.
- 6. New codes, algorithms, code enhancement, and code fixes.** This category is self-explanatory but includes significant changes to existing codes, such as applicability extensions, algorithm optimization, problem correction, limitation removal, or other performance improvement. **Note: Code (or algorithm) capability descriptions are not acceptable, unless they contain sufficient technical material to justify consideration.**
- 7. Code input/output issues.** This normally involves innovations in input (such as input geometry standardization, automatic mesh generation, or computer-aided design) or in output (whether it be tabular, graphical, statistical, Fourier-transformed, or otherwise signal-processed). Material dealing with input/output database management, output interpretation, or other input/output issues will also be considered for publication.
- 8. Computer hardware issues.** This is the category for analysis of hardware capabilities and limitations in meeting various types of electromagnetics computational requirements. Vector and parallel computational techniques and implementation are of particular interest.

Applications of interest include, but are not limited to, antennas (and their electromagnetic environments), networks, static fields, radar cross section, shielding, radiation hazards, biological effects, electromagnetic pulse (EMP), electromagnetic interference (EMI), electromagnetic compatibility (EMC), power transmission, charge transport, dielectric and magnetic materials, microwave components, MMIC technology, remote sensing and geophysics, communications systems, fiber optics, plasmas, particle accelerators, generators and motors, electromagnetic wave propagation, non-destructive evaluation, eddy currents, and inverse scattering.

Techniques of interest include frequency-domain and time-domain techniques, integral equation and differential equation techniques, diffraction theories, physical optics, moment methods, finite differences and finite element techniques, modal expansions, perturbation methods, and hybrid methods. This list is not exhaustive.

A unique feature of the Journal is the publication of unsuccessful efforts in applied computational electromagnetics. Publication of such material provides a means to discuss problem areas in electromagnetic modeling. Material representing an unsuccessful application or negative results in computational electromagnetics will be considered for publication only if a reasonable expectation of success (and a reasonable effort) are reflected. Moreover, such material must represent a problem area of potential interest to the ACES membership.

Where possible and appropriate, authors are required to provide statements of quantitative accuracy for measured and/or computed data. This issue is discussed in "Accuracy & Publication: Requiring quantitative accuracy statements to accompany data", by E.K. Miller, *ACES Newsletter*, Vol. 9, No. 3, pp. 23-29, 1994, ISBN 1056-9170.

EDITORIAL REVIEW

In order to ensure an appropriate level of quality control, papers are refereed. They are reviewed both for technical correctness and for adherence to the listed guidelines regarding information content. Authors should submit the initial manuscript in draft form so that any suggested changes can be made before the photo-ready copy is prepared for publication.

JOURNAL COPY INFORMATION

March issue	Copy deadline 13 January
July issue	Copy deadline 25 May
November issue	Copy deadline 25 September

STYLE FOR CAMERA-READY COPY

The ACES Journal is flexible, within reason, in regard to style. However, certain requirements are in effect:

1. The paper title should NOT be placed on a separate page. The title, author(s), abstract, and (space permitting) beginning of the paper itself should all be on the first page. The title, author(s), and author affiliations should be centered (center-justified) on the first page.
2. An abstract is REQUIRED: The abstract should state the computer codes, computational techniques, and applications discussed in the paper (as applicable) and should otherwise be usable by technical abstracting and indexing services.
3. Either British English or American English spellings may be used, provided that each word is spelled consistently throughout the paper.
4. Any commonly-accepted format for referencing is permitted, provided that internal consistency of format is maintained. As a guideline for authors who have no other preference, we recommend that references be given by author(s) name and year in the body of the paper (with alphabetical listing of all references at the end of the paper). Titles of Journals, monographs, and similar publications should be in boldface or italic font or should be underlined. Titles of papers or articles should be in quotation marks.
5. Internal consistency shall also be maintained for other elements of style, such as equation numbering. As a guideline for authors who have no other preference, we suggest that equation numbers be placed in parentheses at the right column margin.
6. The intent and meaning of all text must be clear. For authors who are NOT masters of the English language, the ACES Editorial Staff will provide assistance with grammar (subject to clarity of intent and meaning).
7. Unused space should be minimized. Sections and subsections should not normally begin on a new page.

MATERIAL, SUBMITTAL FORMAT AND PROCEDURE

The preferred format for submission and subsequent review, is 12 point font or 12 cpi, double line spacing and single column per page. Four copies of all submissions should be sent to the Editor-in-Chief (see inside front cover). Each submission must be accompanied by a covering letter. The letter should include the name, address, and telephone and/or fax number and/or e-mail address of at least one of the authors.

Only camera-ready original copies are accepted for publication. The term "camera-ready" means that the material is neat, legible, and reproducible. The preferred font style is Times Roman 10 point (or equivalent) such as that used in this text. A double column format similar to that used here is preferred. **No author's work will be turned down once it has been accepted because of an inability to meet the requirements concerning fonts and format.** Full details are sent to the author(s) with the letter of acceptance.

There is NO requirement for India ink or for special paper; any plain white paper may be used. However, faded lines on figures and white streaks along fold lines should be avoided. Original figures - even paste-ups - are preferred over "nth-generation" photocopies. These original figures will be returned if you so request.

While ACES reserves the right to re-type any submitted material, this is not generally done.

PUBLICATION CHARGES

ACES members are allowed 12 pages per paper without charge; non-members are allowed 8 pages per paper without charge. Mandatory page charges of \$75 a page apply to all pages in excess of 12 for members or 8 for non-members. Voluntary page charges are requested for the free (12 or 8) pages, but are NOT mandatory or required for publication. A priority courtesy guideline, which favors members, applies to paper backlogs. Full details are available from the Editor-in-Chief.

COPYRIGHTS AND RELEASES

Each primary author must sign a copyright form and obtain a release from his/her organization vesting the copyright with ACES. Forms will be provided by ACES. Both the author and his/her organization are allowed to use the copyrighted material freely for their own private purposes.

Permission is granted to quote short passages and reproduce figures and tables from an ACES Journal issue provided the source is cited. Copies of ACES Journal articles may be made in accordance with usage permitted by Sections 107 or 108 of the U.S. Copyright Law. This consent does not extend to other kinds of copying, such as for general distribution, for advertising or promotional purposes, for creating new collective works, or for resale. The reproduction of multiple copies and the use of articles or extracts for commercial purposes require the consent of the author and specific permission from ACES. Institutional members are allowed to copy any ACES Journal issue for their internal distribution only.